Morphological parameters investigation of deposits formed on pleated filters using DLA

Alexandre Lecoanet, Soleiman Bourrous

Morphological parameters investigation of deposits formed on pleated filters using DLA

A. Lecoanet[a], S. Bourrous[a,*]

[a]*Institut de Radioprotection et de Sûreté Nucléaire (IRSN), PSN-RES/SCA/LECEV, F-91400, Saclay, France*

Abstract

Pleated filters are widely used as they offer a greater filtration area, leading to lower pressure losses. However, their geometry impacts the air flow fields inside their pleats, which can evolve as more aerosol matter accumulates. This leads to different behavior between flat and pleated filters with respect to pressure loss evolution with both filtration velocity and deposited mass. To study the effect of streamlines inclination on deposit morphology, the possibility of producing numerical deposits is here investigated. A custom DLA code is used, which can handle both poly-dispersed particle populations and streamline tilt for spherical particles. The DLA approach is particularly relevant for studying pleated filters as it accurately captures the complex interplay between particle deposition dynamics, porosity evolution, and flow field modifications, which are critical for understanding clogging behavior and optimizing filter performance. The morphological parameters here considered are the porosity, the contact angle distribution, and the coordination number distribution. The DLA approach, by accounting for stochastic and deterministic forces, is well-suited for simulating nanoparticle behavior where Brownian motion is significant. It provides detailed insights into deposit microstructures and the influence of pleat geometry and flow incidence angles, offering a powerful tool for advancing both theoretical models and practical applications in aerosol filtration systems. Computations

*Corresponding author
Email address: soleiman.bourrous@irsn.fr (S. Bourrous)

were carried out to reproduce experimental results on porosity obtained with mono-dispersed PSL and poly-dispersed CsCl particles. Comparisons show good agreement between the experimental porosities and those computed using the custom DLA code. Contact angles and coordination number distributions give physically coherent results. Theoretical probability density functions for the contact angle distributions in both the diffusion and ballistic regimes were obtained and shown to agree with the distributions numerically obtained. Based on the adequacy between simulation results and experimental data, the effect of streamlines tilt on deposit porosity was investigated. In the simulations carried out, inclination of gas flow direction increases the limiting porosity in the ballistic regime when the tilt is higher than 45° with respect to the capture plane normal vector.

Keywords: DLA, HEPA filters, porosity, contact angle, coordination number, poly-dispersed, pleated filters, streamlines tilt

---

1. Nomenclature

.

Latin letters

B_v	Coefficient linked to brownian motion	$\sqrt{\frac{2k_bT_{air}}{m_p\tau_p}}$	$m.s^{-3/2}$	[1]
CMD	Count median diameter	-	m	[2]
Cu	Cunningham coefficient	$1+Kn\,[1.257$ $+0.4exp\left(-\frac{1.10}{Kn}\right)]$	-	Davies 1945 in [3]
d_0	Reference diameter	10^{-9}	m	[2]
D_b	Stokes-Einstein diffusion coefficient	$\frac{Cuk_bT_{air}}{3\pi\mu_{air}d_p}$	$m^2.s^{-1}$	[3]
d_p	Particle diameter	-	m	-
$E_B\,[\theta]$	Contact angle expected value in ballistic regime	-	rad	-
$E_D\,[\theta]$	Contact angle expected value	-	rad	-

	in diffusion regime			
f	Friction coefficient	$\frac{3\pi\mu_{air}d_p}{Cu}$	$kg.s^{-1}$	-
$\mathrm{f_B}$	Theoretical ballistic contact angle probability density function	-	$\#.rad^{-1}$	Appendix B
$\mathrm{f_D}$	Theoretical diffusion contact angle probability density function	-	$\#.rad^{-1}$	Appendix A
F_{ext}	External force	-	N	[4]
J	Porosity correlation shape factor	-	-	[5]
k_b	Boltzmann's constant	$1.38 \cdot 10^{-23}$	$J.K^{-1}$	-
Kn	Knudsen number	$\frac{2\lambda_{air}}{d_p}$	-	-
L_f	Filter side length	-	m	-
L_f^*	Scaled filter side length	$\frac{L_f}{CMD}$	-	-
m_p	Particle mass	$\frac{\pi}{6}\rho_p d_p^3$	-	-
$\mathcal{N}(a,b)$	Normal distribution with mean a and standard deviation b	-	-	-
N_c	Coordination number	-	$\#$	-
N_p	Number of particles	-	$\#$	-
N_R	Number of repeats	-	$\#$	-
p	Probability	-	-	-
P_0	Standard pressure	101 325	Pa	-
Pe	Peclet number	$\frac{d_p V_f}{D_b}$	-	-
P_{air}	Air pressure	-	Pa	-
R	Random force	-	N	[4]
R_p	Particle radius	$\frac{d_p}{2}$	m	-
Stk	Stokes number	$\frac{Cu\rho_p d_p V_f}{9\mu_{air}}$	-	-
t	Time	-	s	-
T_0	Standard temperature	273.15	K	-

T_{air}	Air temperature	-	K	-
U_p	Particle velocity	-	$m.s^{-1}$	-
V_f	Fluid velocity	-	$m.s^{-1}$	-
W	Wiener process	-	$kg.s^{-1/2}$	[1]
X_p	Particle position	-	m	-
Z_{max}	Z position of the deposit which is the furthest from the filter	-	m	-
Z^*	Scale deposit height	$\left\|\frac{Z}{d_p}\right\|$	-	-

Greek letters

α	Streamline tilt	-	^{o}	-
Δ	Difference / Absolute uncertainty	-	-	-
Δt	Time step	-	s	[1]
ε	Porosity	-	-	-
ε_b	Porosity in full ballistic regime	-	-	-
ε_d	Porosity in full diffusion regime	-	-	-
θ	Contact angle	-	rad	-
λ_{air}	Air molecules mean free path	$21.55\mu_{air}\frac{\sqrt{T_{air}}}{P_{air}}$	m	[6]
λ_p	Particle mean free path	$\frac{\sqrt{m_p k_b T_{air}}}{f}$	m	[7]
μ_{air}	Dynamic viscosity of air	$1.496 \cdot 10^{-6}\frac{T_{air}^{1.5}}{T_{air}+120}$	$Pa.s$	[6]
ρ_{air}	Air density	$1.293 \times 273.15\frac{P_{air}}{T_{air}P_0}$	$kg.m^{-3}$	Ideal gas
ρ_p	Particle density	-	$kg.m^{-3}$	-
σ	Standard deviation	-	-	-
σ_g	Geometric standard deviation	-	-	[2]
τ_p	Particle relaxation time	$\frac{Cu\rho_p d_p^2}{18\mu_{air}}$	s	[4]
ξ_χ, ξ_ν	Vector of 3 elements in $\mathcal{N}(0,1)$ representing randomness of particle	-	-	[1]

	position and velocity

Indices

air	Air
max	Maximum
p	Particle

2. Glossary

$DALEC$	*Dépôt par aggrégation Limité par la diffusion pour l'Etude du Colmatage*
DLA	Diffusion Limited Agregation
$HEPA$	High-Efficiency Particulate Air
$LECEV$	Laboratoire d'Expérimentations sur le Comportement des Equipements et de la Ventilation
$LIMA$	Laboratoire Interactions Media Aérosols
$LRGP$	Laboratoire Réactions et Génie des Procédés
PSL	Polystyrene Latex particle
SCA	Service du Confinement et de l'Aérodispersion des polluants

3. Introduction

. Pleated filters are widely used, in diverse domains spanning from vacuum cleaner to automotive industry or nuclear industry. The reason is that they offer an increased filtration surface leading to a lower filtration velocity and therefore lower pressure losses. This boon however comes at a price. Pleated filters show a non-linear dependency of pressure drop on filtration velocity [8, 9, 10, 11] as well as on deposited mass [12] & [13]. This dependency is function of pleats geometry [9, 14]. This deviation can be partially imparted to streamlines constriction with the pleats[15, 16].

In addition to this deviation from the linear case of Darcy, they are prone to early clogging. Deposited mater tends to form arch, see Saleh *et al.* simulation

results [17] and [8]. These empty space entrapped this way can be called a macroscopic porosity, which was also studied by Alilou [18]. This macroscopic porosity comes in addition to the structural porosity. The overall porosity is therefore higher leading to a lower lifetime of the filter.

. Also, during pleated filters clogging, segregation of particles can occur [14]. It stems from difference in ability of particles to follow streamline deviations, which is measured by their higher Stokes number, Stk. For particles of the same nature, the ones with a bigger diameter will tend to accumulate at pleat end while the smaller ones will tend to follow the streamlines closely and spread all over the pleat. This implies that particles accumulation is not homogeneous throughout the pleat. Particle segregation is also a function of pleats geometry [14].

. All phenomena listed influence the morphology of the deposits formed in a pleated filter, at both the local scale and the global scale. Different zones of the same pleat can be subjected to different particle populations due to segregations. Also the streamlines may not plunge into the filter and the deposit in the same way, and it can change overtime due to the change in the porous structure induced by particle accumulation. Conducting experimental investigation of deposit morphology inside the pleats of a filter is difficult. To overcome experimental limitations, numerical study needs to be carried on.

. For the simulation study of filters clogging two main approach were investigated [19]. The first is based on 3-D microscale modelling [7, 20, 19] in which each particles trajectories and collisions are solved. The main advantage is that the entire deposit is obtained. It requires prior knowledge of the laden flow field and pressure loss are calculated afterward. The second approach is based on 1-D macroscale pressure drop models [19, 17] for which particles are treated as a concentration and deposit in cells of the meshed domain. When particles deposit in a cell it increases the cells particle concentration, up to when they reach their maximum solid volume fraction. They become blocked and parti-

cles deposit in the neighboring cells. It requires experimental data and / or microscale simulations to determine the deposition rates of particles in the cells as well as the maximum solid volume fraction. The main advantage is here that large domains can be computed, with convoluted shapes. Also, pressure drop is directly obtained and its influence on the flow can be readily taken into account.

. In this piece of work, the focus is on the possibility to study deposit microstructure via 3-D microscale modelling approach when the laden flow arrives with a normal or a tilted incidence. First attempts to use DLA to study deposit growth date back to the pioneer work of Tassopoulos *et al.* [21]. In their work particles move from cell to cell on a square grid. They are put in motion by a superposition of a deterministic force and of a stochastic force modeling Brownian motion. Mädler *et al.* [7] numerically studied the deposits formed of mono-dispersed spherical particles and aggregates of such particles under thermophoresis using DLA approach. Elmøe *et al.* [20] also successfully used Langevin [4] to simulate capillary clogging. More recently DLA approach was used by Dépée *et al.* [22] to study scavenging of aerosol particles by rain drops in clouds.

. We focus on nanoparticles for which Brownian motion cannot be neglected. Porosity of deposits formed by such particles are scarce. The work of Nuvoli *et al.* [23] can however be cited. They measured porosity of deposits formed by aggregation of nanoparticles and aggregates of nanoparticles on a flat filter. The laden air flow crossed the filtration medium at right angle. In addition, they have shown that the Stokes number (Stk) was more appropriate to describe porosity (ε) evolution than the Peclet number (Pe). From their experiments, they obtained an empirical correlation, equation (1).

$$\varepsilon = \varepsilon_d + \frac{(\varepsilon_b - \varepsilon_d)\, Stk}{J + Stk} = 0.9876 + \frac{(0.82979 - 0.9876)\, Stk}{0.06498 + Stk} \tag{1}$$

. The three morphological parameters investigated here are the deposit porosity, particles contact angles distribution and particles coordination numbers distri-

bution. The porosity is the main factor influencing pressure drops and also the clogging rate of pleated filters. Contact angles distributions and coordination numbers distributions give quantitative descriptions of the way particles deposit on each other. As indirect measures of particles deposition their study could lead to analytic clogging models. Coordination number is also linked to deposit resistivity which is important for gas detector, for instance.

. Here the focus is on the surface filtration, where the particles accumulate outside of the filtration medium. First the code used is presented, as well as the post-processing methods used to obtain the three morphological parameters investigated here: deposit porosity, contact angle distribution an coordination number distribution. The code was written in Python 3 [24] and mainly used Numpy [25] and Scipy [26] libraries. Then, the code is applied to two sets of experimental conditions used by Nuvoli *et al.* [23]. The first one was performed with mono-dispersed spherical PSL, the second one was performed with poly-dispersed spherical CsCl particles. Porosities are compared Contact angles and coordination number distributions are analyzed. Contact angle distributions are also confronted to asymptotic theoretical distributions presented in Appendix B & Appendix A. It is the first time, to the best of our knowledge, that DLA computations are applied to filtration with poly-dispersed particles and compared to experimental results. After the experimental validation, the effect of inclination of the laden gas direction with respect to the capture plane on deposit porosity and contact angles and coordination numbers distributions is studied.

4. Methods

4.1. Computation domain

. Particles are entrained by air flow toward an impenetrable capture plane which represents the filter. Particles are assumed to be spherical with diameter d_p. Agglomeration of particles before they reach the deposited layer or the filter is neglected. To amounts to assume that particles are diluted in the gas.

. The computational domain is schematically depicted in figure 1.Along Oz axis, the domain is closed on the capture side by an impenetrable plane simulating the filter, and it is open on the other side. Periodic boundary conditions are applied on the sides of the domain. To account for periodic conditions with poly-dispersed particles populations we used ghost particles. These particles simulate the presence of particle which exceed domain bounds through the planes on which periodic boundary conditions are applied.

. Particles drop plane is not fixed, but follow deposit growth. Particles are dropped from a plane placed just further away from the deposit. The drop margin is computed so that the biggest particle cannot touch the deposit. The distance between the biggest particle and the top of the deposit is equal to 5 % of the biggest particle radius. This margin is lower than that used by Mädler *et al.* [7], who used a margin of 60 d_p. We tried the two approaches and did not observe any change in the morphological parameters we study here. This is also coherent with the fact that Brownian motion is a Markov process. Particle position is set at random within the drop plane.

. Air is assumed to flow upward along +Oz. The flow can arrive at an angle to account for streamline tilt.

. In the code, the particles population is considered to be poly-dispersed following a log-normal distribution, see [2]. In order to avoid arising from unrealistically small or large particles the range of diameters was reduced to the following interval. According to the properties of the log-normal distribution, this interval only leaves out 0.3 % of the distribution.

$$\frac{CMD}{\sigma_g^3} < d_p < CMD \times \sigma_g^3 \tag{2}$$

The width of the domain, L_f, was here determined by sensitivity analysis. $L_f^* = \frac{L_f}{CMD} = 60$ was used here.

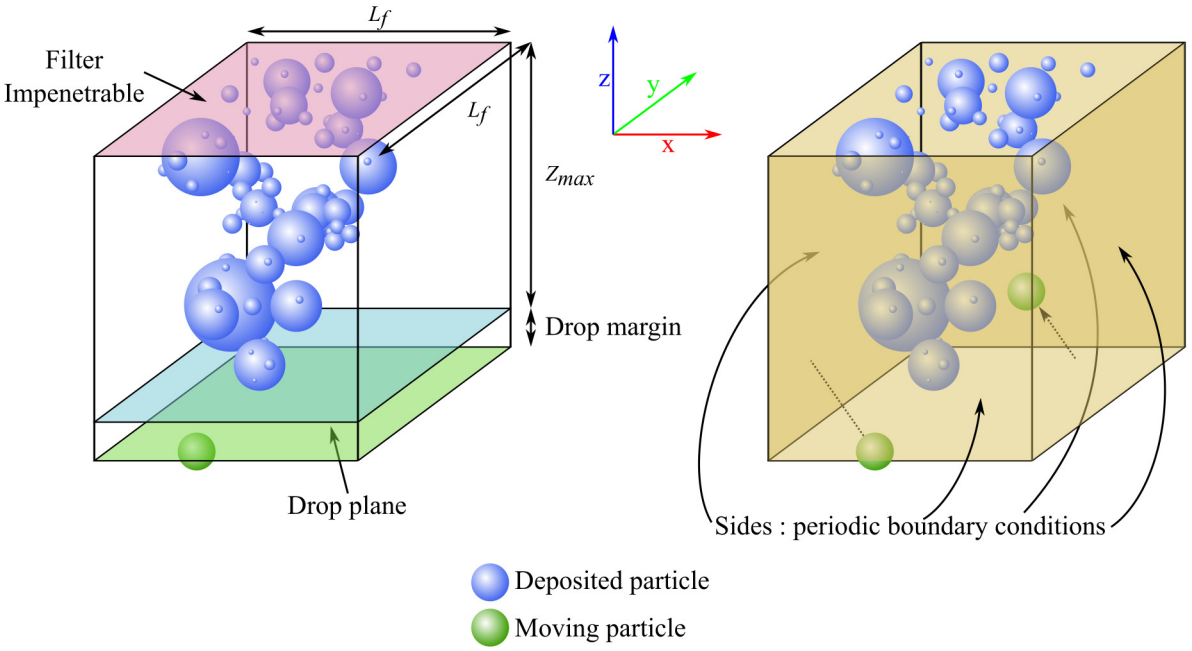

Figure 1: Schematic description of computation domain.

4.2. Equations of motion

. Lagrangian approach of Langevin [4] is used to simulate particle motion. It can be summarized by Eq. (3). It takes into account both the average effect of gas molecule interaction with the particle, *i.e.* the drag force, and the random effect, $\boldsymbol{R}$, due to the small number of interactions induced by relative size of particle and gas molecule mean free path. τ_p is the particle relaxation time.

$$m_p \frac{\mathrm{d}\boldsymbol{U_p}(t)}{\mathrm{d}t} = -\frac{m_p}{\tau_p}\left[\boldsymbol{V_f} - \boldsymbol{U_p}(t)\right] + \boldsymbol{R} + \boldsymbol{F_{ext}} \tag{3}$$

Equation (3) can here be rewritten as equation (4), where B_v is the diffusion coefficient due to Brownian motion and $\mathrm{d}\boldsymbol{W}(t)$ is the the Wiener process increment which is used to model a random walk to approximate Brownian motion of the particle.

$$\begin{cases} \mathrm{d}\boldsymbol{X_p}(t) = \boldsymbol{U_p}(t)\mathrm{d}t \\ \mathrm{d}\boldsymbol{U_p}(t) = \dfrac{1}{\tau_p}\left[\boldsymbol{V_f} - \boldsymbol{U_p}(t)\right]\mathrm{d}t + B_v \mathrm{d}\boldsymbol{W}(t) \end{cases} \tag{4}$$

Due to the stochastic nature of equation (4) it cannot be solved directly. To solve this equation the analytical Lagrangian integration scheme by Minier *et al.* [1] is used. This scheme, summarized by equations (5), gives from a given position and velocity of a particle, its position and velocity after a time-step of Δt. It can be applied for both short time steps, $\Delta t << \tau_p$, corresponding to ballistic motion and for large time steps, $\Delta t >> \tau_p$, corresponding to diffusive motion. The stochastic nature of the scheme is carried by the two vectors $\boldsymbol{\xi_\chi}$ and $\boldsymbol{\xi_\nu}$ which elements are random variables following the normal distribution $\mathcal{N}(0,1)$. This scheme was successfully applied in previous studies like the one of Dépée *et al.* [22], on aerosol scavenging by water droplets.

$$\begin{cases} \boldsymbol{X_p}(t+\Delta t) = \boldsymbol{X_p}(t) + \boldsymbol{U_p}(t)\tau_p\left(1 - e^{-\frac{\Delta t}{\tau_p}}\right) + \boldsymbol{V_f}\left[\Delta t - \tau_p\left(1 - e^{-\frac{\Delta t}{\tau_p}}\right)\right] \\ \qquad + B_v\tau_p\sqrt{\Delta t - \dfrac{2\tau_p\left(1 - e^{-\frac{\Delta t}{\tau_p}}\right)}{\left(1 - e^{-\frac{\Delta t}{\tau_p}}\right)}}\boldsymbol{\xi_\chi} \\ \qquad + B_v\tau_p^2\dfrac{\left(1 - e^{-\frac{\Delta t}{\tau_p}}\right)^2}{\sqrt{2\tau_p\left(1 - e^{-\frac{2\Delta t}{\tau_p}}\right)}}\boldsymbol{\xi_\nu} \\ \boldsymbol{U_p}(t+\Delta t) = \boldsymbol{U_p}(t)e^{-\frac{\Delta t}{\tau_p}} + \boldsymbol{V_f}\left(1 - e^{-\frac{\Delta t}{\tau_p}}\right) + B_v\sqrt{\dfrac{\tau_p}{2}\left(1 - e^{-\frac{2\Delta t}{\tau_p}}\right)}\boldsymbol{\xi_\nu} \end{cases} \tag{5}$$

Eventhough Minier *et al.* [1] scheme is valid for all values of Δt it must be chosen with care when deposit formation is been studied. As stated by Tassopoulos *et al.* [21] and Mädler *et al.* [7] the particle mean free path, λ_p has an impact on deposit microstructure. A particle with a lower mean free path is more likely to be captured and it generate more porous deposit. If the Δt used is too high with respect to λ_p then some part of the particle displacement will be missed and it is less likely to be captured. Therefore, if Δt value too high then the compacity of the deposit produced will be artificially high. To

overcome this hurdle a dimensionless time step, Δt^* Eq. (6), indexed on the main driving force, V_f, the fluid velocity and λ_p was defined. A practical value, Eq. (6), was determined by sensitivity analysis and confirmed by confrontation with experiments, *cf.* section 5.1.

$$\Delta t^* = \frac{\Delta t V_f}{\lambda_p} = \frac{1}{40} \tag{6}$$

4.3. Post-processing

. Deposit visualizations were used for qualitative analysis. These visualizations were made using ParaView software [27]. For quantitative analysis Python3 [24] was used (DALEC_PostTraitement). The focus was on three morphological parameters :

- The porosity ε;
- The contact angle between particles;
- The coordination numbers of particles.

. To compute the local porosity of the deposit was sliced by 3 000 planes and for each slice the porosity was taken equal to the ratio of the surface not in a particle too the total surface of the slice. As the capture plane is an idealization from the real case the first slices are not representative of the deposit. Likewise for the lat slices the deposit is not established. Therefore, to compute the average porosity of the deposit and its standard-deviation, only the porosity of the slices between $20 \times CMD$ and 50 % of the total height of the deposit.

. For each particles touching at least another one, the contact location is measured here as the angle between the equatorial plane[1] and the contact point. Only positive values are considered to avoid counting the same contact twice. Therefore, the contact angles ranges here from 0^o if the contact point is on the

[1] *i.e. the plane parallel to the filter surface passing by the center of the particle.*

equatorial plane and 90^o if the contact point is at the pole of the touched particle. A theoretical probability density function, f, was obtained, see Appendix Appendix B. The histograms are here all compared to f.

The distribution of contact angles of the particles gives an indication on how the particles are captured. Indeed, if particles stack one above the others, *i.e.* at 90^o from particle equatorial plane, the deposit will be more porous than if they preferentially stack side by side, *i.e.* at 0^o from particle equatorial plane.

. For every particle in the deposit, the number of particles it is in contact with is determined to give a distribution. The distribution of coordination numbers gives a measure of the deposit morphology as a contact number of 2 corresponds to a particle in a linear chain while coordination number of one is a chain termination and contacts angles above two correspond to particle at a fork.

5. Results & discussion

. In this section the results obtained are presented in two parts. The first one focuses on experimental confrontation with experiments carried out with mono-dispersed and poly-dispersed spherical particles. The second one deals with the effect of flow direction tilt on morphological parameters.

5.1. Experimental confrontation

. DLA code are often compared to each other [7], but often suffer from a lack of experimental confrontation. That is why our code is confronted here to experiments carried out by Nuvoli *et al.* [5, 23].

5.1.1. Mono-dispersed PSL particles

. Nuvoli *et al.* [5, 23] performed experiments with spherical PSL. These particles had a CMD of 64 nm. The experimental conditions tested by Nuvoli *et al.* [5, 23] are summarized in table 1, along with the porosity, ε, which was the main results of these experiments.

. Calculations were launched for the same gas velocity as for the experiments, see table 1. All relevant parameters used for the calculations are summarized in table 2. All particles generated had the same diameter; σ_g was set to 1.

. The porosity evolution with the absolute scaled distance from the filter, $Z^* = \left|\frac{Z}{d_p}\right|$, for all the calculations are given in figure 2. The two establishment zones are visible for low and high values of Z^*. The first spans roughly up to between $Z^* = 10$ and $Z^* = 20$ while the second one begins at $Z^* = Z^*_{max} - 20$. The analysis zone is located outside the establishment zone. Therefore, no bias was introduced by this means in the porosity calculations.

. Figure 3 show the evolution of the average deposit porosity, ε, with Stokes number, Stk, as obtained via the computations along side the one obtained from experimental results from Nuvoli *et al.* [5, 23] and the one given by Nuvoli *et al.* [5, 23] correlation, equation (1). Visualizations of three deposits formed in the diffusive regime, V0, the transition regime, V2, and the ballistic regime are given in figure 3.

For $V \geqslant V2$ the computations reproduce accurately the the both the measured values as well as the ones from the correlation. The computed values are within the experimental uncertainties, or the experimental point, V4, lies inside the dispersion interval around the computed values. For V0 and V1, the computed values for ε are similar to the ones obtained with correlation (1), but they are far from the experimental ones. The correlation was obtained on a larger batch of experiments with more diverse conditions. Therefore, experimental bias is suspected and the results from the correlation is deemed more truth worthy.

. DLA can thus be used to construct numerical deposit of mono-dispersed particles which porosities are coherent with real deposits.

. As our code can reproduce macroscopic morphological parameter of the PSL deposits, the porosity porosity, it is possible to go further and analyze the contact angles distributions as well as the coordination numbers distributions.

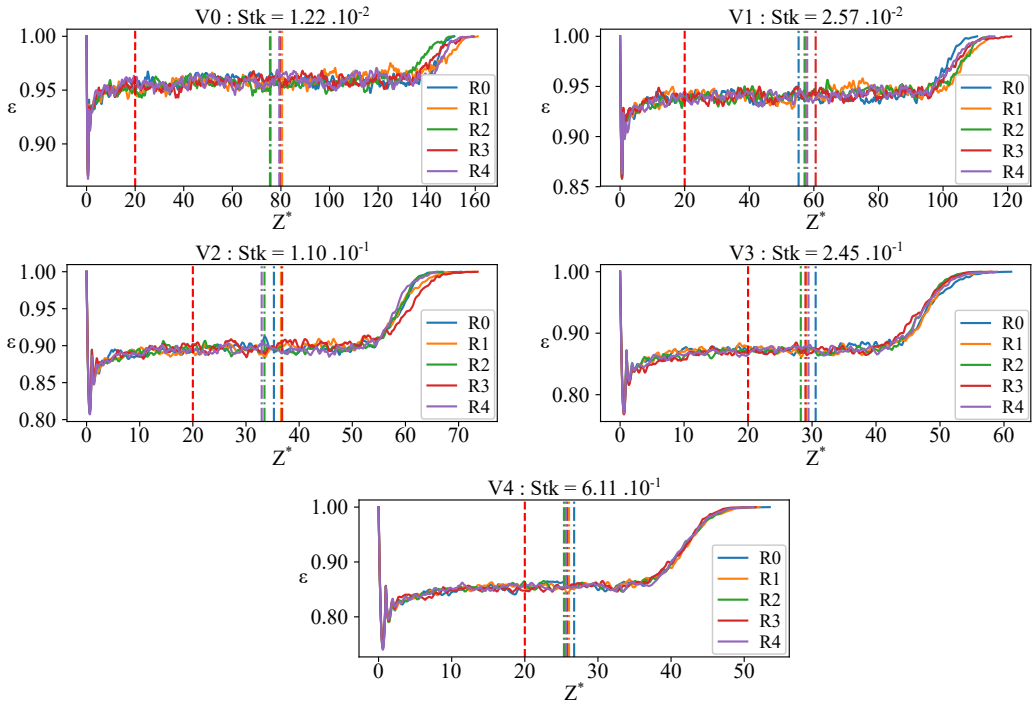

Figure 2: Porosity evolution for PSL with scaled deposit height, Z^* for every repetition of every calculation corresponding to tables 1 & 2. Red vertical discontinuous line represents the lower bound used for mean porosity evaluation, see section 4.3. Other discontinuous lines represent the higher bound used for mean porosity evaluation, see section 4.3.

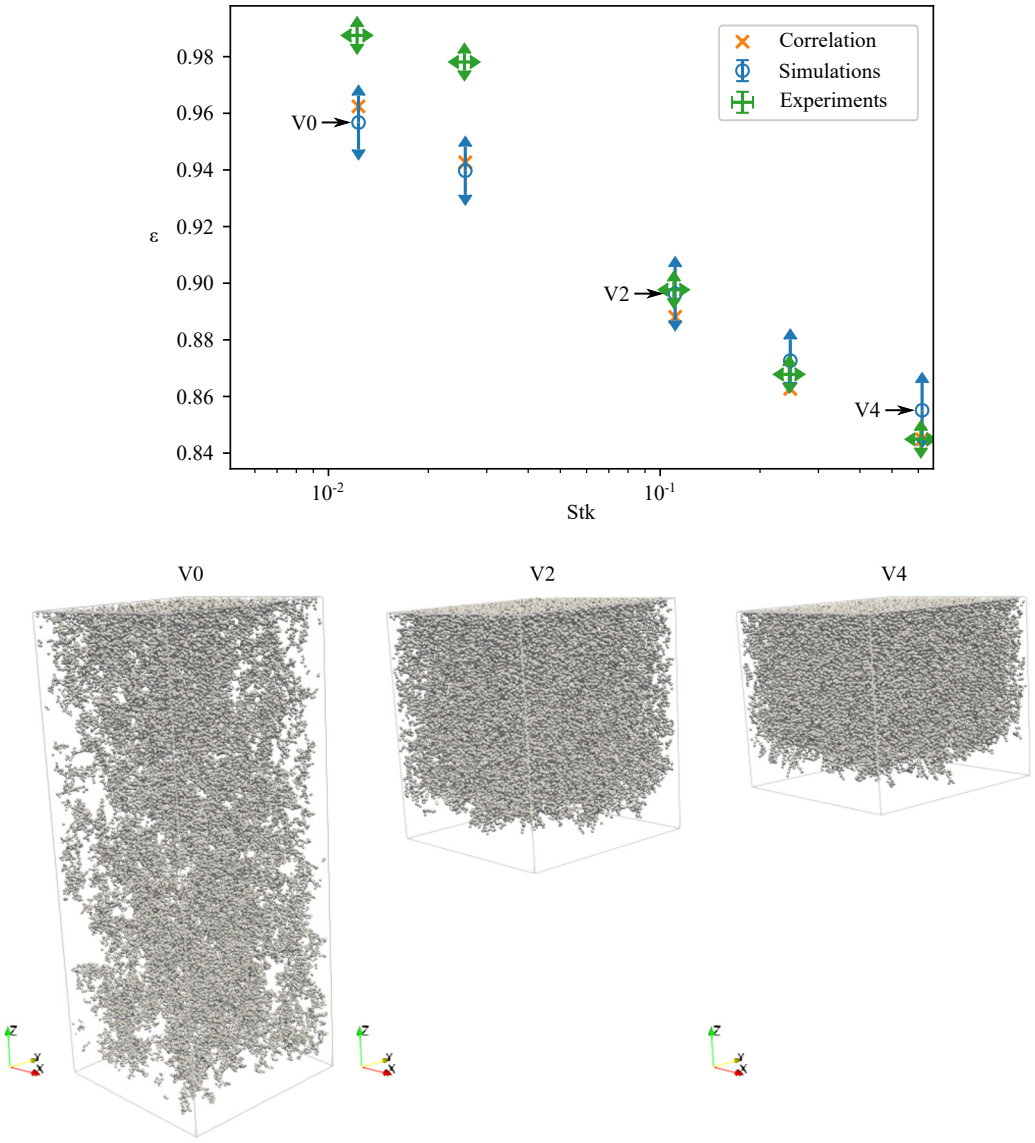

Figure 3: Top: Porosity evolution with Stk for PSL particles, considering input parameters in tables 1 & 2, according to the simulations, to correlation (1), and to experiments presented in [23] & [5]. Confidence intervals on experimental points are pictured by means of arrows. Arrows on simulations represent dispersion $2\sigma_\varepsilon$. Bottom: Deposit visualization for the first repeat calculations for V0, V2 and V4 obtained with ParaView. 3D representations of the three deposits showed here are available as ".ply" files in supplementary materials.

Index	V_f $[m.s^{-1}]$	σ_{V_f} $[m.s^{-1}]$	Pe $[-]$	σ_{Pe} $[-]$	Stk $[-]$	σ_{Stk} $[-]$	ε $[-]$
V0	$7.34 \cdot 10^{-3}$	$3.3 \cdot 10^{-5}$	0.314	$6.1 \cdot 10^{-3}$	$1.22 \cdot 10^{-2}$	$2.4 \cdot 10^{-4}$	0.988
V1	$1.54 \cdot 10^{-2}$	$6.9 \cdot 10^{-5}$	0.66	$1.3 \cdot 10^{-2}$	$2.57 \cdot 10^{-2}$	$5.0 \cdot 10^{-4}$	0.978
V2	$6.61 \cdot 10^{-2}$	$3.0 \cdot 10^{-4}$	2.83	$5.5 \cdot 10^{-2}$	$1.10 \cdot 10^{-1}$	$2.1 \cdot 10^{-3}$	0.898
V3	$1.47 \cdot 10^{-1}$	$6.6 \cdot 10^{-4}$	6.3	$1.2 \cdot 10^{-1}$	$2.45 \cdot 10^{-1}$	$4.7 \cdot 10^{-3}$	0.868
V4	$6.67 \cdot 10^{-1}$	$1.6 \cdot 10^{-3}$	15.7	$3.0 \cdot 10^{-1}$	$6.11 \cdot 10^{-1}$	$1.2 \cdot 10^{-2}$	0.845

Table 1: Porosity obtained by Nuvoli [5] for PSL with $CMD = 64\ nm$ and $\sigma_g = 1.1$, along with the corresponding experimental parameters. The uncertainty on ε is $\Delta\varepsilon = 0.003$.

CMD $[nm]$	σ_g $[-]$	ρ_p $[kg.m^{-3}]$	T_{air} K	P_{air} $[Pa]$	N_p $[\#]$	Rep $[\#]$
64	1	1 050	293.15	101 325	43 200	5

Table 2: Parameters used for computations performed for confrontation with Nuvoli [5] experiments with PSL, see table 1.

The contact angles distributions are available in figure 4 for the PSL deposits numerically created. Confidence intervals are narrower than the differences between two sets of computations carried out on different gas velocities. Evolution in distributions are therefore significant and can be analyzed. Going from the lower to the higher Stk values, the mod shifts from around 0 ^{o} to around 45 ^{o}. The average contact angle, which are given in table 3, increase as well, while the attached standard deviation stays the same. Distribution shape evolves with Stk. When Stk decreases the distribution tends toward the theoretical limit for a pure diffusion regime, as presented in Appendix A while when Stk increases the distribution tends toward the theoretical limit for ballistic regime, as presented in Appendix B. The tendency is also noticed on the average contact angles gathered in table 3 which shift from 34 ^{o} for the lowest Stk values to 43 ^{o} for the highest ones. These values agree with the mathematical expectancies for pure diffusion, $E_D[\theta] = 32.7\ ^o$ see. Appendix A, as well as for the ballistic regime, $E_B[\theta] = 45\ ^o$ see. Appendix B. A difference between the diffusion and

the ballistic regimes is that in ballistic regime the angle mode and average are identical as this is not true in diffusion regime.

From another point of view, we can note that the increase in frequency of contact angles of around 0^o for lower values of Stk are coherent with the increase in lateral movements of particle with respect to the flow in diffusion regime. So the limit distribution of contact angles for both low and high Stk values can be physically explained and were theoretically modeled. It builds confidence in the physical adequacy of the deposit created. It also means that reduced values like the average contact angles given in 3 can be used for global description of the deposit.

Index	θ $[^o]$	σ_θ $[^o]$
V0	34	22
V1	35	22
V2	37	22
V3	40	22
V4	43	21

Table 3: Mean and standard-deviation of contact angles distributions obtained on PSL computations, see table 1 & 2.

. The last microstructural parameter studied here is the coordination number, N_c. Coordination numbers distributions computed on numerically obtained PSL deposits are given in figure 5. The confidence intervals are narrower than most evolutions witnessed. The maximum coordination number observed is of 6 when the theoretical maximum is 8. These results are therefore, plausible. Confidence intervals on coordination numbers of 5 and 6 mostly include 0 in frequency. They are left aside for the analysis. With an increase in Stk comes an increase in relative frequencies of coordination numbers 0 and 2, and a decrease in all other coordination numbers. $N_c = 0$ corresponds to particles that passed through the deposit without touching it. The probability for this to happen increases when

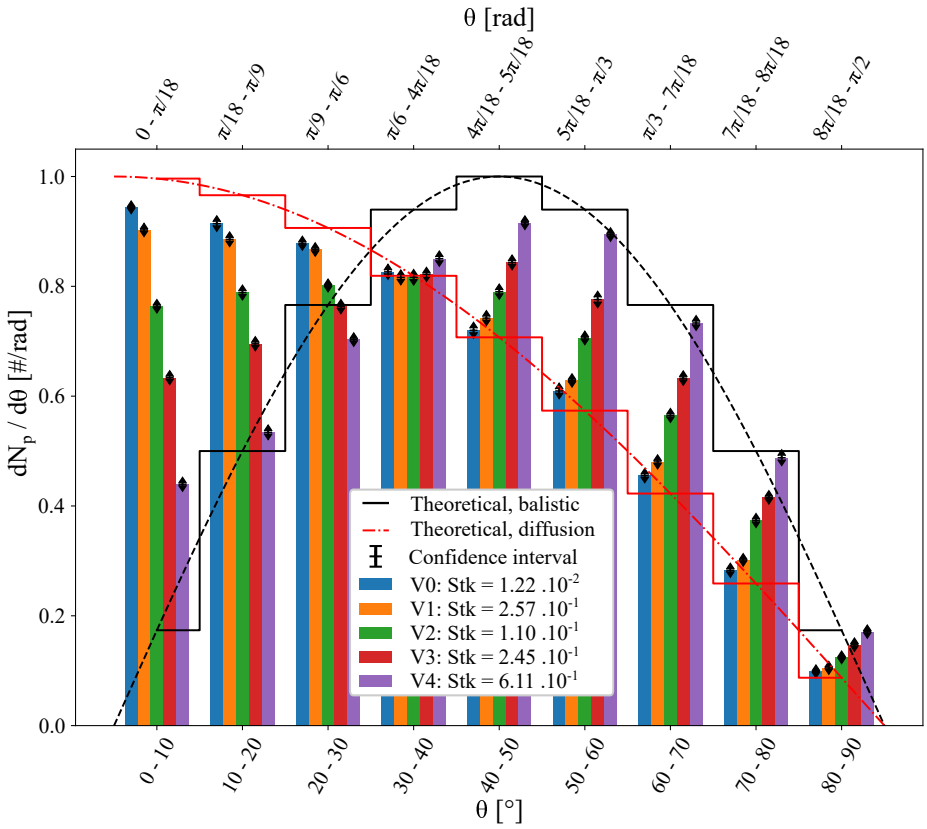

Figure 4: Contact angles histogram for simulations conducted using PSL, *cf.* tables 1 & 2. Confidence intervals are given as black arrows. The theoretical probability function in ballistic regime presented in appendix Appendix B is represented in continuous form as a dotted black line, and in the histogram form as a solid black line. The theoretical probability function in diffusion regime presented in appendix Appendix A is represented in continuous form as a dashed-dotted red line, and in the histogram form as a solid red line.

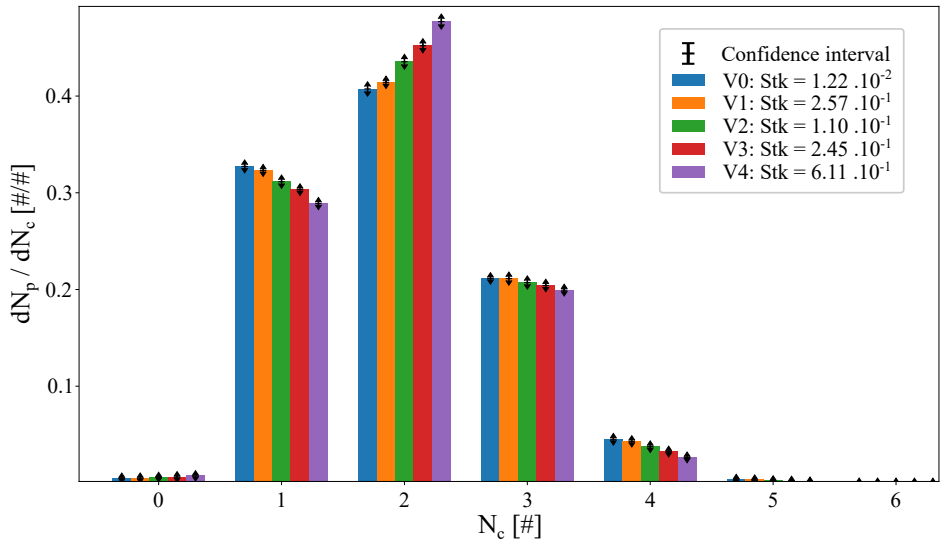

Figure 5: Coordination numbers histograms for simulations conducted using PSL, *cf.* tables 1 & 2. Confidence intervals are given as black arrows.

the particle travels in a straight line; so in ballistic regime. Likewise, particles with $N_c = 2$ are parts of linear chains of particles. These linear chains can form when particle pile on top of each other. These two N_c are coherent with ballistic transport at high Stk values. Conversely, $N_c > 2$ correspond to a particle at a fork. More particle with $N_c > 2$ indicates a more branched structure, with each branch terminated by a particle with $N_c = 1$. So increase in $N_c = 1$ and $N_c > 2$ are coherent with a diffusion transport regime of particles. The coordination numbers distribution limit trends are compatible with the expected physical transport regimes.

5.1.2. Poly-dispersed CsCl particles

. Our DLA approach was tested on CsCl poly-dispersed particles populations experimentally investigated by Nuvoli *et al.* [5, 23]. The main experimental parameters along with the measured porosities are summarized in table 4. CsCl particle are spherical and in Nuvoli *et al.* [23] experiments, their size distribution followed a log-normal distribution. Particle population parameters are gathered

in table 5 along with the numerical parameters used. An example of particles size distributions used for computations is available in figure 6. They are compared to the theoretical distribution. The numerically generated distributions are in adequacy with the theoretical one. The generation limits are also displayed on figure 6, see equation (2).

Index	V_f $\left[m.s^{-1}\right]$	σ_{V_f} $\left[m.s^{-1}\right]$	Pe $[-]$	σ_{Pe} $[-]$	Stk $[-]$	σ_{Stk} $[-]$	ε $[-]$
V0	$4.09 \cdot 10^{-4}$	$8.2 \cdot 10^{-6}$	$1.6 \cdot 10^{-2}$	$2.2 \cdot 10^{-3}$	$2.6 \cdot 10^{-3}$	$3.6 \cdot 10^{-4}$	0.974
V1	$1.64 \cdot 10^{-3}$	$3.3 \cdot 10^{-5}$	$6.4 \cdot 10^{-2}$	$9.0 \cdot 10^{-3}$	$1.0 \cdot 10^{-2}$	$1.4 \cdot 10^{-3}$	0.965
V2	$8.19 \cdot 10^{-3}$	$1.6 \cdot 10^{-4}$	$3.2 \cdot 10^{-1}$	$4.5 \cdot 10^{-2}$	$5.2 \cdot 10^{-2}$	$7.2 \cdot 10^{-3}$	0.913
V3	$3.27 \cdot 10^{-2}$	$6.6 \cdot 10^{-4}$	1.3	$1.8 \cdot 10^{-1}$	$2.1 \cdot 10^{-1}$	$2.9 \cdot 10^{-2}$	0.870
V4	$1.47 \cdot 10^{-1}$	$6.6 \cdot 10^{-4}$	5.7	$8.0 \cdot 10^{-1}$	$9 \cdot 10^{-1}$	$1.3 \cdot 10^{-1}$	0.840
V5	$5.87 \cdot 10^{-1}$	$2.6 \cdot 10^{-3}$	23	3.2	3.7	$5.1 \cdot 10^{-1}$	0.840

Table 4: Porosity obtained by Nuvoli [5] for CsCl particles with $CMD = 62\ nm$ and $\sigma_g = 1.75$, along with the corresponding experimental parameters. The uncertainty on ε is $\Delta\varepsilon = 0.003$.

CMD $[nm]$	σ_g $[-]$	ρ_p $\left[kg.m^{-3}\right]$	T_{air} K	P_{air} $[Pa]$	N_p $[\#]$	Rep $[\#]$
62	1.75	3 990	293.15	101 325	15 000	5

Table 5: Parameters used for computations performed for confrontation with Nuvoli [5] experiments with CsCl particles, see table 4.

. Porosity (ε) evolution with Z^* is available for all calculations in figure 7. The two establishment zones are always visible. They spans up to $Z^* = 20$ for the first one and from $Z^* = Z^*_{max} - 30$ for the second one. Their size is greater than for the mono-dispersed case, see figure 2. This could be a polydispersion effect as well as the effect of a reduction in number of particles. Computations were done with more particles during prototyping of domain size and number of particles, and the increase of the second establishment zone from $Z^* = Z^*_{max} - 20$ to $Z^* = Z^*_{max} - 30$, was also witnessed for computations with a greater number of

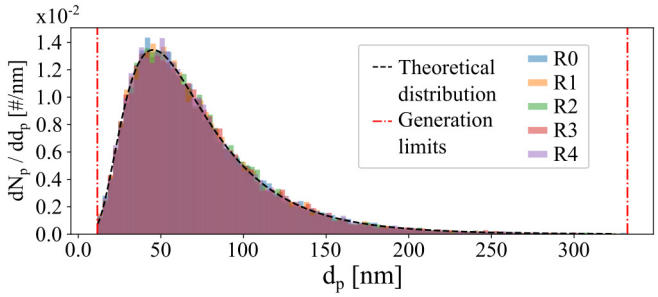

Figure 6: CsCl particle size distributions for the 5 simulations with V0, *cf.* tables 4 & 5. The generation limits are pictures as vertical discontinuous red lines, see equation (2). The theoretical distribution is represented as a discontinuous black line.

particles. The number of particles was reduced when poly-dispersed particles were considered because of computation time and deposit height. The final goal is here to investigate the effect of streamline tilt, and computations without tilt are used later in the present piece of work as a comparison point. To put aside effect of numbers of particles, the computations should be conducted with the same number of particles. Streamline tilt induces a drastic increase in computational time. To keep the time reasonable with tilt and maintain the same number of particles, the number of particles was reduced. The height of deposit is higher in the poly-dispersed case compared to the mono-dispersed case. It is one of the reasons the number of particles could be reduced.

Compared to mono-dispersed case presented here, see figure 2, porosity evolution with deposit height in the poly-dispersed case, see figure 7, is more volatile. This is due to both the reduction in particle number and to the poly dispersion.

In between the considered analysis limits, see section 4.3, the porosity is stable.

. Figure 8 gives porosity evolution with Stk as computed from the numerical deposits produced by the code, as computed using correlation (1), as measured by Nuvoli *et al.* [23], along with three examples of numerical deposits. Arrows around simulations values indicate dispersion, while the one around the exper-

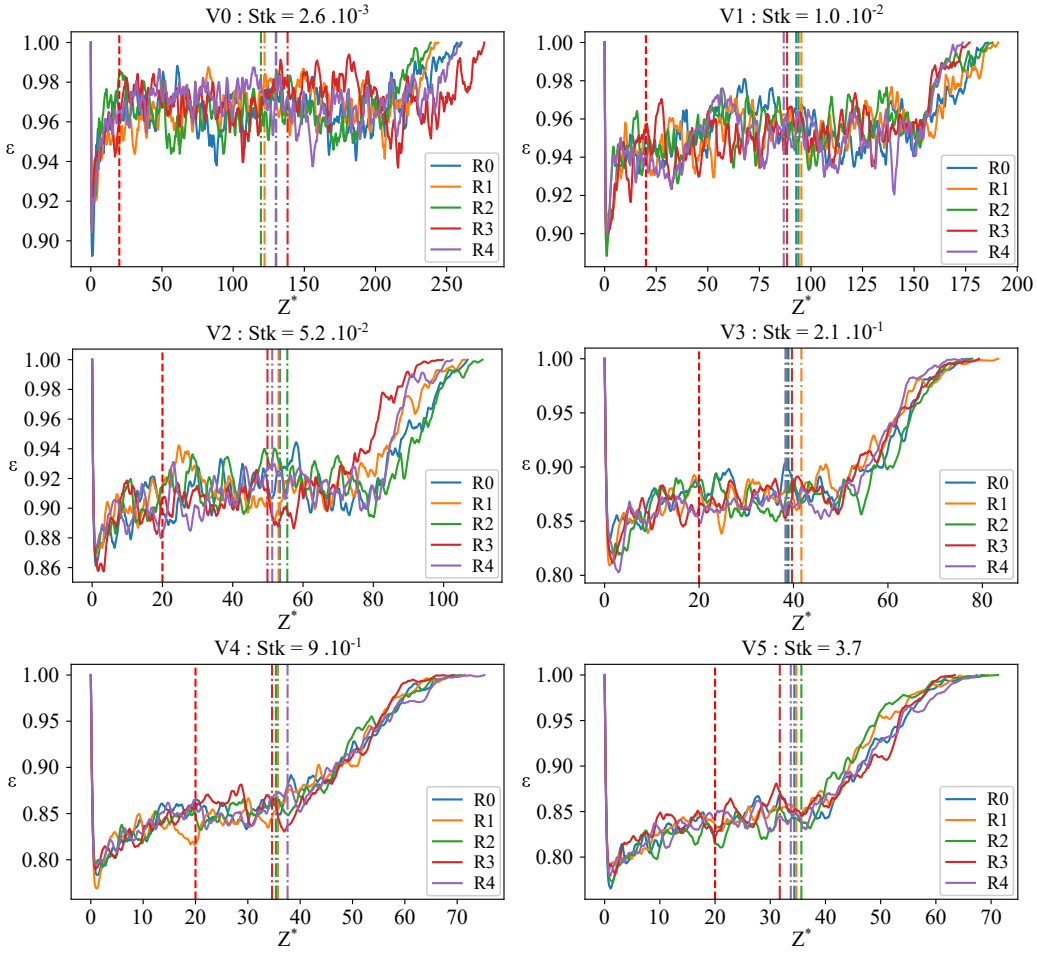

Figure 7: Porosity evolution for CsCl particles with scaled deposit height, Z^* for every repetition of every calculation corresponding to tables 4 & 5. Red vertical discontinuous line represents the lower bound used for mean porosity evaluation, see section 4.3. Other discontinuous lines represent the higher bound used for mean porosity evaluation, see section 4.3.

imental points picture the confidence intervals. For 4 out of the 6 investigated sets of conditions, the simulations values are within the experimental confidence intervals. For the remaining 2 the experimental points are within the dispersion around the simulations values. It appears as the change between the diffusion and the transition regime as well as the change between the transition regime and the ballistic regime are anticipated by the simulations. Likewise, for 4 out of the 6 investigated sets of conditions, the simulations values are closer to the experimental points than correlation (1). In conclusion our approach allows for accurate computation of deposit porosity in the three main regimes: diffusion, transition, ballistic.

. Contact angle distributions computed for CsCl simulations are available in figure 9. As noted for mono-dispersed PSL the distributions tends toward the diffusion and ballistic theoretical limits which are presented respectively in Appendix A & Appendix B. The average and standard deviation of contact angles are given in table 6. The values are bounded by the theoretical mathematical expectancies for both the diffusion regime, $E_D[\theta] = 32.7\ ^o$ see. Appendix A, for low Stk values and the ballistic regime, $E_B[\theta] = 45\ ^o$ see. Appendix B. The adequacy is better than for mono-dispersed PSL.

Index	θ [^{o}]	σ_θ [^{o}]
V0	33	22
V1	33	22
V2	34	22
V3	36	22
V4	40	22
V5	44	21

Table 6: Mean and standard-deviation of contact angles distributions obtained on CsCl particles computations, see table 4 & 5.

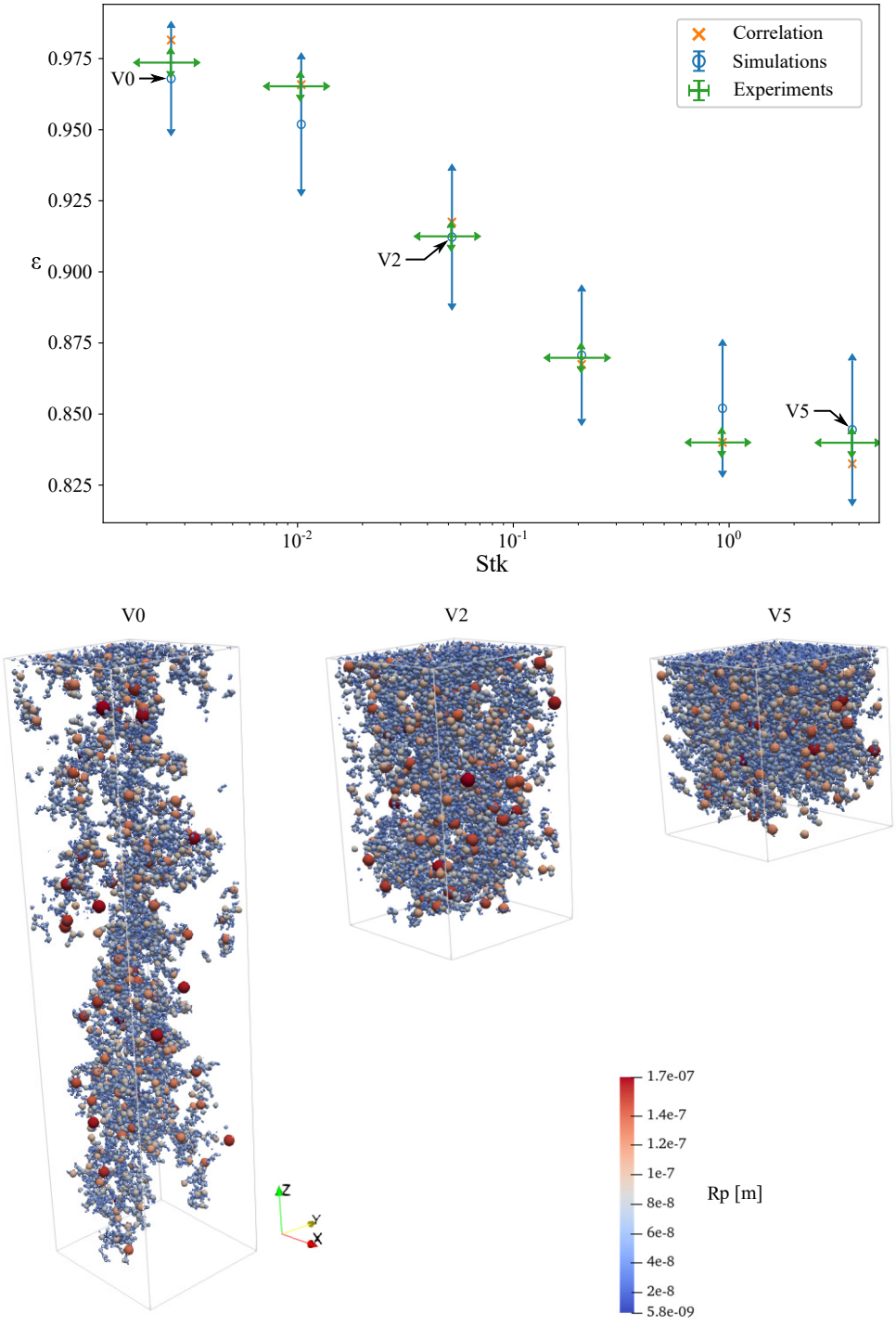

Figure 8: Top: Porosity evolution with Stk for CsCl particles, considering input parameters in tables 4 & 5, according to the simulations, to correlation (1), and to experiments presented in [23] & [5]. Confidence intervals on experimental points are pictured by means of arrows. Arrows on simulations represent dispersion $2\sigma_\varepsilon$. Bottom: Deposit visualization for the first repeat calculations for V0, V2 and V5 obtained with ParaView. 3D representations of the three deposits showed here are available as ".ply" files in supplementary materials.

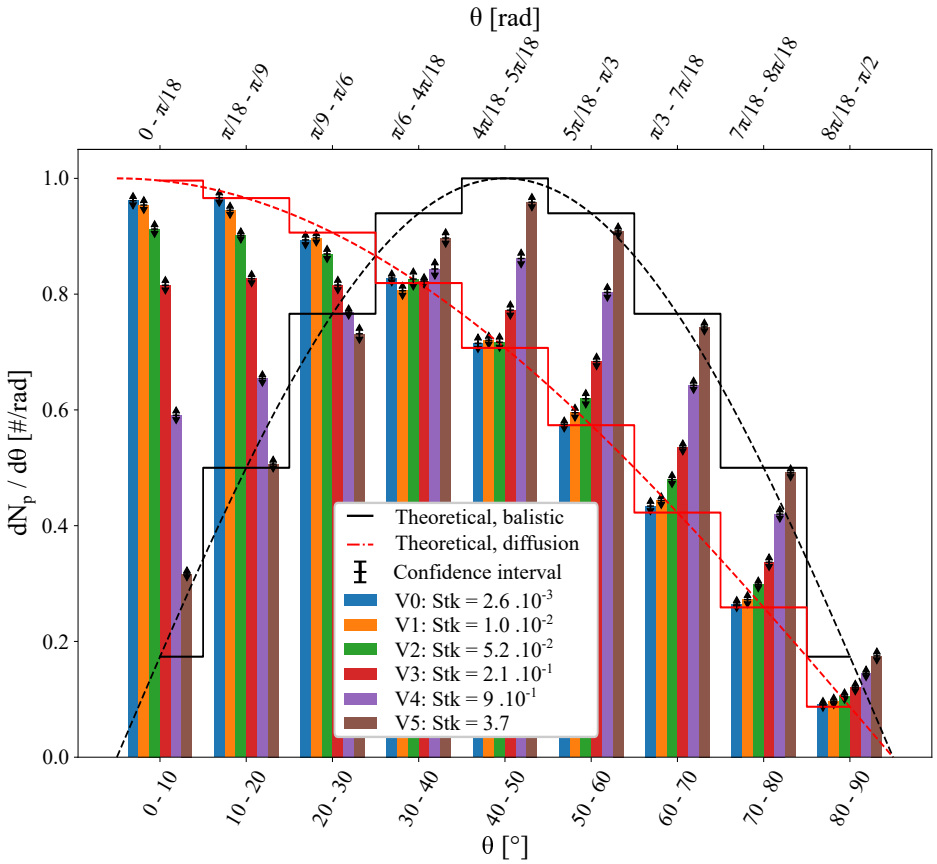

Figure 9: Contact angles histogram for simulations conducted using CsCl particles, *cf.* tables 4 & 5. Confidence intervals are given as black arrows. The theoretical probability function in ballistic regime presented in appendix Appendix B is represented in continuous form as a dotted black line, and in the histogram form as a solid black line. The theoretical probability function in diffusion regime presented in appendix Appendix A is represented in continuous form as a dashed-dotted red line, and in the histogram form as a solid red line.

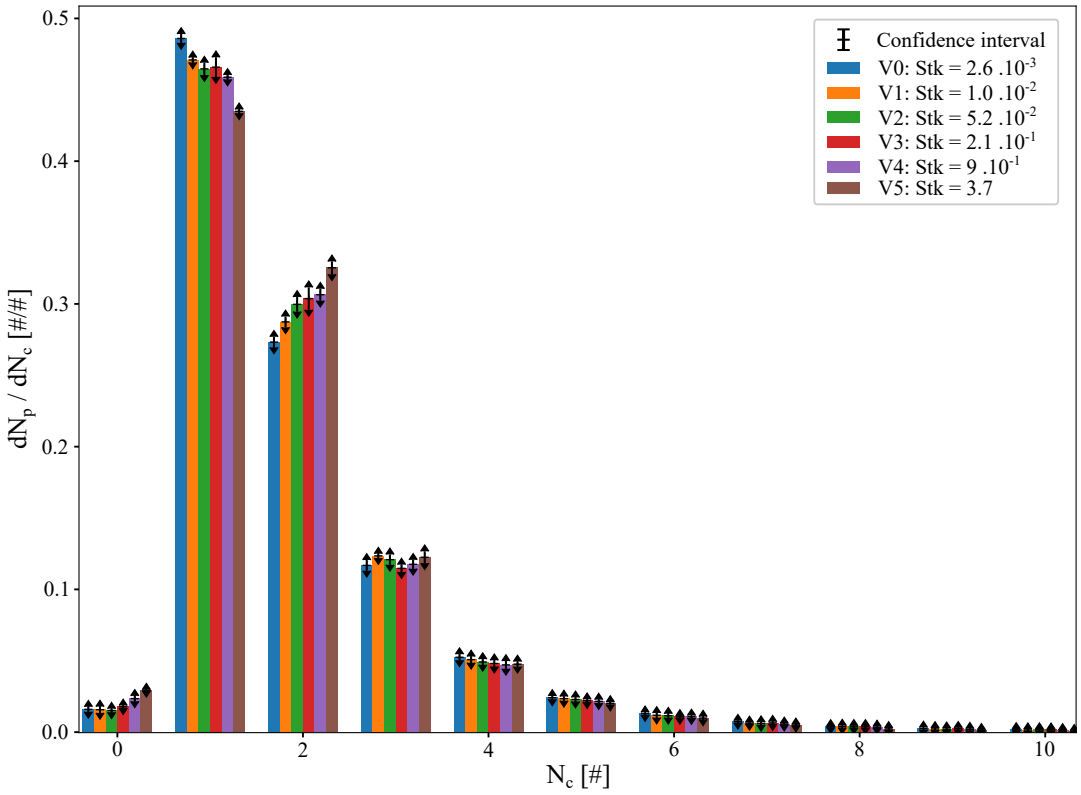

Figure 10: Coordination numbers histogram for simulations conducted using CsCl, *cf.* tables 4 & 5. Confidence intervals are given as black arrows. Parts of the histograms with $N_c > 10$ were left out.

. Coordination numbers histograms are reported in figure 10. The maximum coordination number encountered was of 30. However, frequencies for $N_c > 10$ show no visible evolution with Stk and their confidence intervals limits are close to 0 therefore this part of the diagram was left out. This is one of the differencies between mono-dispersed and poly-dispersed particles populations that the maximum coordination is no longer 8, and is mush higher. Another difference is that $N_c = 3$ frequency seems unaffected by Stk variations. The global description is the same, as lower Stk lead to more arborescent structures typical of diffusion process, while higher values of Stk lead to more linear structures typical of ballistic accumulation.

5.2. Streamlines tilt effect on deposit

. To study the effect of gas streamline tilt for a poly-dispersed population of particles, the same CsCl particle population is considered as well as the same numerical parameters as in previous section, see tables 4 & 5. The only change is the tilt, α, of the gas flow with respect to the normal to the capture plane. In addition to the previous case $\alpha = 0\ ^o$, 7 other values were investigated $\alpha \in [5\ ^o, 15\ ^o, 30\ ^o, 45\ ^o, 60\ ^o, 75\ ^o, 85\ ^o]$[2].

. All contact angles distributions obtained for different values of α investigated are gathered in Appendix C. No effect of α on the contact angles distributions is witnessed. Likewise, all coordination numbers distributions obtained for different values of α investigated are gathered in Appendix D. No effect of α on the coordination numbers distributions is witnessed. Therefore, here the focus is on the effect of α on porosity. Porosity results are plotted against Stk in figure 11. Visualizations of 4 deposits obtained from different values of α and V_f are given in figure 12. To extract asymptotic porosity values in diffusion, ε_d, and ballistic, ε_b regimes non-linear curve-fitting[3] was applied to $\varepsilon = g\,(Stk)$ data for each tested value of α. The type of function assumed for the non-linear curve-fitting is the same as correlation (1). The unknowns are ε_d, ε_b, and J. To initialize the non-linear curve-fitting procedure correlation (1) were used. $\varepsilon = g\,(Stk)$ resulting from the non-linear curve-fitting procedures are also displayed in figure 11. Values of ε_d and ε_b along with their confidence intervals are plotted against α in figure 13.

. In diffusion regime $Stk << 1$, data points in figure 11 are close to each other. Also, the deposit formed are similar, see figure 12. Finally, all the confidence intervals of ε_d overlap, see figure 13. ε is unaffected by α. The lower the Stk, likewise the lower the Peclet number, the lower the effect of inertia compared to

[2] $\alpha = 0\ ^o$ means that the flow is normal to the capture plane, while $\alpha = 90\ ^o$ means that the flow is parallel to the capture plane.

[3] Scipy.optimize.curve_fit from Scipy 1.2.1 was used.

diffusion. Therefore, the fact that ε_d is unaffected by streamline tilt is physically valid.

. In ballistic regime $Stk \geqslant 1$, the effect of α is not linear. For $\alpha \leqslant 45\ ^o$, no significant variation of ε_b is visible on figure 11 & 13. For $\alpha > 45\ ^o$, a significant increase of ε_b is blatant on figure 11 & 13. This follows from a structural changes in the deposit formed as can be seen by comparing deposits formed at V5 with respectively $\alpha = 45\ ^o$ and with $\alpha = 85\ ^o$ in figure 12. When streamlines are tilted, already deposited particles prevent moving particles to deposit behind them. This leads to higher ε_d values. For the limiting case $\alpha = 90\ ^o$, the only transport mechanism for particles to reach the deposit surface is diffusion. Therefore, in this case $\varepsilon_b = \varepsilon_d$. One ca note that confidence intervals of $\varepsilon_b\,(\alpha = 85\ ^o)$ and $\varepsilon_d\,(\alpha = 75\ ^o)$ overlap, meaning that $\varepsilon_b\,(\alpha = 85\ ^o) = \varepsilon_d\,(\alpha = 75\ ^o)$. The evolution of ε_b with α observed is coherent with the physical interpretations given.

.

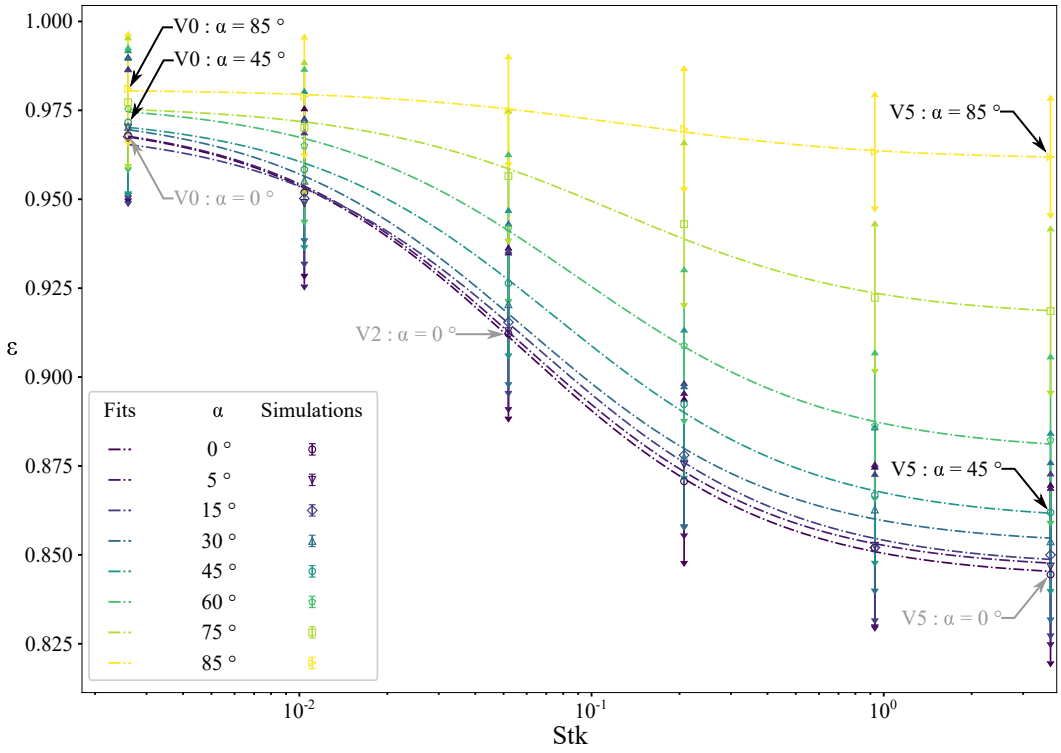

Figure 11: Porosity evolution with Stk for the calculations performed with different flow direction tilts. Arrows correspond to porosity dispersion ($2\sigma_\varepsilon$). Lines correspond to fits of porosity results for each tilt. Deposits corresponding to the four points labeled in black ($\alpha = 45\ ^o$ & $\alpha = 85\ ^o$) are available in figure 12. Deposits corresponding to the three points labeled in grey ($\alpha = 0\ ^o$) are available in figure 8.

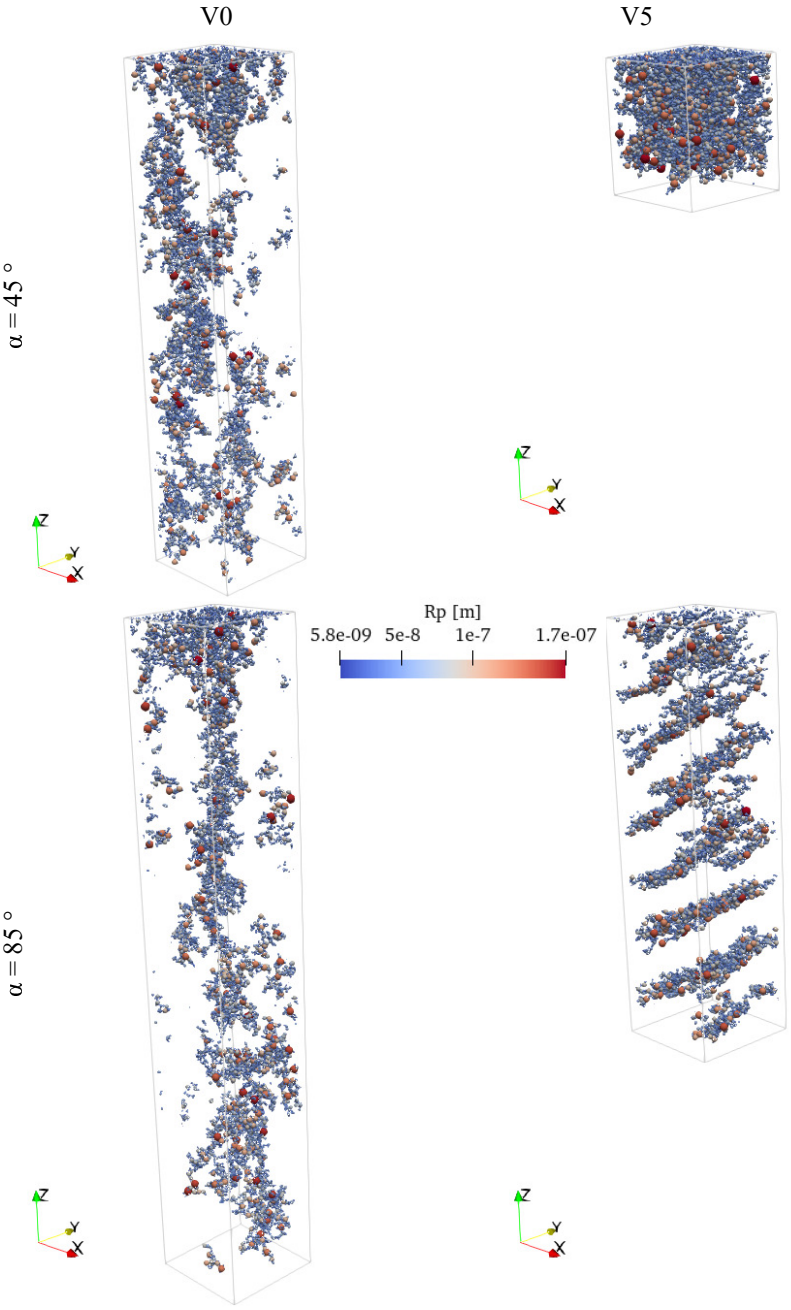

Figure 12: Visualizations of deposits corresponding to V0 and V5, see tables 4 & 5 , with $\alpha = 45\ ^o$ and $\alpha = 85\ ^o$. 3D representations of the four deposits showed here are available as ".ply" files in supplementary materials.

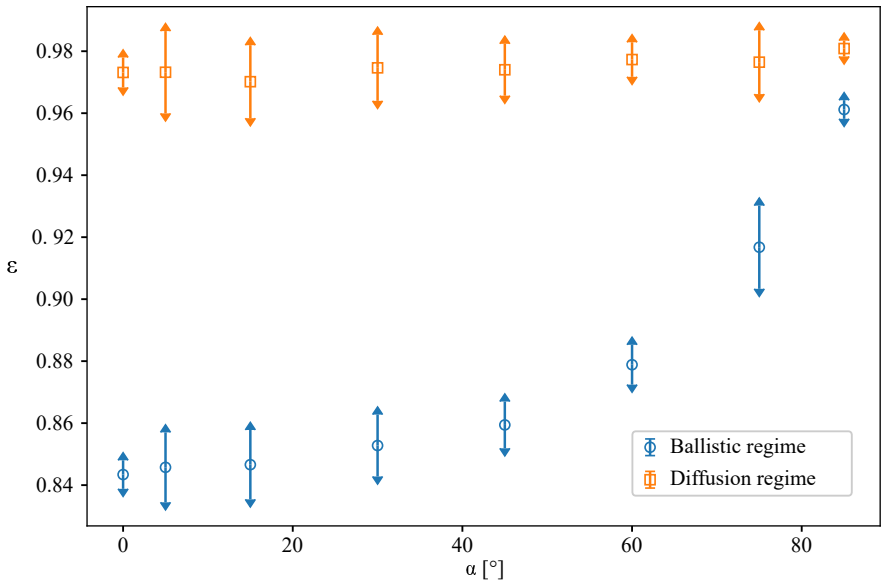

Figure 13: Evolution of limit porosity in diffusion regime, ε_d, and in ballistic regime, ε_b, as a function of streamline tilt from normal incidence. Confidence intervals are represented using arrows.

6. Conclusion

. The aim of the present piece of work is to study the possible use of DLA code to study microsctructural parameters of deposits produced by filtration of poly-dispersed spherical particles transported by an air flow arriving on the capture plane with a tilt.

. It was shown that a DLA approach with periodic boundary conditions can produce numerical deposits which porosity matches experimental porosity data for both monododispersed and poly-dispersed particles. Other microsctructutal parameters were studied, *i.e.* contact angles distribution and coordination numbers distributions. These data are difficult to achieve experimentally. The distributions obtained from analysis of the numerical deposits are physically credible. Realistic theoretical models were obtained for contact angle distributions in both diffusion, see Appendix A, and ballistic, see Appendix B, regimes. They match numerical simulations results.

. Investigation of streamlines tilt showed that neither does it affects the contact angles distributions nor the coordination numbers distributions. It does not affects the limit porosity in diffusion regime, ε_d. However, it does affects the limit porosity in ballistic regime, ε_b, where a threshold effect is witnessed. For $\alpha \leqslant 45\ ^o$, ε_b stays unaffected, but for $\alpha > 45\ ^o$, ε_b increases and tends toward ε_d. This increase can, if it occurs to early clogging of pleated filters.

. Data on contact angles could be used as a basis for global porosity models for HEPA pleated filter for instance. Segregation and surface reduction can occur during pleated filters clogging. Flow fields inside the filters pleats can therefore change as more aerosol matter is deposited. Porosity can therefore evolve in time and within the pleat. Coupling DLA codes like the one used here to CFD could help solve this problem and give accurate numerical simulations capable of handling the effect of deposit microsctructural changes throughout the clogging process on the pressure drop as well as on the clogging itself. Dynamic porosity

maps could be generated. This in turn could lead to better design of aerosol filtration units, and better operations practices.

7. Acknowledgments

This work is a part of the LIMA joint research program between the Institut de Radioprotection et de Sûreté Nucléaire (IRSN) and the Reactions and Chemical Engineering Laboratory (LRGP) of the French National Center for Scientific Research (CNRS) and the Lorraine University.

8. Declaration of competing interest

The authors declare that they have no known competing financial interests or personal relationships that could have appeared to influence the work reported in this paper.

References

[1] J.-P. Minier, E. Peirano, The pdf approach to turbulent polydispersed two-phase flows, Physics Reports 352 (1) (2001) 1–214. doi:https://doi.org/10.1016/S0370-1573(01)00011-4.
URL https://www.sciencedirect.com/science/article/pii/S0370157301000114

[2] W. C. Hinds, Aerosol Technology, 2nd Edition, Wiley-Interscience, New York, NY, USA, 1999.

[3] H. R. Pruppacher, J. D. Klett, Microphysics of Clouds and Precipitation, 2nd Edition, Kluwer academic publishers, 1998.

[4] P. Langevin, Sur la théorie du mouvement brownien, Compte rendus de l'académie des sciences de Paris 146 (1908) 530–536.

[5] J. Nuvoli, Étude des mécanismes de formation des dépôts de particules appliquée à la filtration THE, Ph.D. thesis, Université de Lorraine (2021).
URL http://www.theses.fr/2021LORR0049

[6] B. A. Tinsley, L. Zhou, A. Plemmons, Changes in scavenging of particles by droplets due to weak electrification in clouds, Atmospheric Research 79 (3) (2006) 266–295. doi:https://doi.org/10.1016/j.atmosres.2005.06.004.
URL https://www.sciencedirect.com/science/article/pii/S0169809505001602

[7] L. Mädler, A. A. Lall, S. K. Friedlander, One-step aerosol synthesis of nanoparticle agglomerate films: simulation of film porosity and thickness, Nanotechnology 17 (19) (2006) 4783–4795. doi:10.1088/0957-4484/17/19/001.
URL https://doi.org/10.1088/0957-4484/17/19/001

[8] S. Bourrous, Étude du colmatage des filtres THE plans et à petits plis par des agrégats de nanoparticules simulant un aérosol de combustion, Ph.D. thesis, Université de Lorraine (2014).
URL http://www.theses.fr/2014LORR0301

[9] L. Del Fabbro, J.-C. Laborde, P. Merlin, L. Ricciardi, Air flows and pressure drop modelling for different pleated industrial filters, Filtration & Separation 39 (1) (2002) 34–40. doi:https://doi.org/10.1016/S0015-1882(02)80055-6.
URL https://www.sciencedirect.com/science/article/pii/S0015188202800556

[10] M. Rebaï, M. Prat, M. Meireles, P. Schmitz, R. Baclet, Clogging modeling in pleated filters for gas filtration, Chemical Engineering Research and Design 88 (4) (2010) 476–486. doi:https://doi.org/10.1016/j.cherd.2009.08.014.

URL https://www.sciencedirect.com/science/article/pii/S0263876209002214

[11] F. Théron, A. Joubert, L. Le Coq, Numerical and experimental investigations of the influence of the pleat geometry on the pressure drop and velocity field of a pleated fibrous filter, Separation and Purification Technology 182 (2017) 69–77. doi:https://doi.org/10.1016/j.seppur.2017.02.034.
URL https://www.sciencedirect.com/science/article/pii/S1383586616321062

[12] V. Mocho, F.-X. Ouf, Clogging of industrial pleated high efficiency particulate air (HEPA) filters in the event of fire, Nuclear Engineering and Design 241 (5) (2011) 1785–1794, iCONE-17: Heavy Liquid Metal Technologies and Material Challenges for Gen IV Fast Reactors. doi:https://doi.org/10.1016/j.nucengdes.2011.01.036.
URL https://www.sciencedirect.com/science/article/pii/S0029549311000902

[13] F.-X. Ouf, V.-M. Mocho, S. Pontreau, Z. Wang, D. Ferry, J. Yon, Clogging of Industrial High Efficiency Particulate Air (HEPA) Filters in Case of Fire: From Analytical to Large-Scale Experiments, Aerosol Science and Technology 48 (9) (2014) 939–947. arXiv:https://doi.org/10.1080/02786826.2014.947022, doi:10.1080/02786826.2014.947022.
URL https://doi.org/10.1080/02786826.2014.947022

[14] S. Fotovati, S. Hosseini, H. Vahedi Tafreshi, B. Pourdeyhimi, Modeling instantaneous pressure drop of pleated thin filter media during dust loading, Chemical Engineering Science 66 (18) (2011) 4036–4046. doi:https://doi.org/10.1016/j.ces.2011.05.038.
URL https://www.sciencedirect.com/science/article/pii/S0009250911003538

[15] M. Rebaï, M. Prat, M. Meireles, P. Schmitz, R. Baclet, A semi-analytical model for gas flow in pleated filters, Chemical Engineering Science 65 (9)

(2010) 2835–2846. doi:https://doi.org/10.1016/j.ces.2010.01.014.
URL https://www.sciencedirect.com/science/article/pii/S000925091000031X

[16] Y. Alilou, N. Bardin-Monnier, D. Thomas, S. Bourrous, P. Lemaître, T. Gélain, Development of a semi-analytical model to predict the pressure drop of clean pleated high efficiency particulate air filters, The Canadian Journal of Chemical Engineering - (-) (2022, in press) CJCE–20–0836.

[17] A. Saleh, S. Fotovati, H. Vahedi Tafreshi, B. Pourdeyhimi, Modeling service life of pleated filters exposed to poly-dispersed aerosols, Powder Technology 266 (2014) 79–89. doi:https://doi.org/10.1016/j.powtec.2014.06.011.
URL https://www.sciencedirect.com/science/article/pii/S0032591014005543

[18] Y. Alilou, Impact sur le colmatage en régimes transitoire et permanent des écoulements d'air induits par le plissage des médias filtrants THE, Ph.D. thesis, Université de Lorraine (2018).
URL http://www.theses.fr/2018LORR0047

[19] A. Saleh, S. Hosseini, H. Vahedi Tafreshi, B. Pourdeyhimi, 3-d microscale simulation of dust-loading in thin flat-sheet filters: A comparison with 1-d macroscale simulations, Chemical Engineering Science 99 (2013) 284–291. doi:https://doi.org/10.1016/j.ces.2013.06.007.
URL https://www.sciencedirect.com/science/article/pii/S0009250913004144

[20] T. D. Elmøe, A. Tricoli, J.-D. Grunwaldt, S. E. Pratsinis, Filtration of nanoparticles: Evolution of cake structure and pressure-drop, Journal of Aerosol Science 40 (11) (2009) 965–981. doi:https://doi.org/10.1016/j.jaerosci.2009.09.002.
URL https://www.sciencedirect.com/science/article/pii/S0021850209001621

[21] M. Tassopoulos, J. A. O'Brien, D. E. Rosner, Simulation of microstructure/mechanism relationships in particle deposition, AIChE Journal 35 (6) (1989) 967–980. doi:https://doi.org/10.1002/aic.690350610.
URL https://aiche.onlinelibrary.wiley.com/doi/abs/10.1002/aic.690350610

[22] A. Dépée, P. Lemaitre, T. Gelain, A. Mathieu, M. Monier, A. Flossmann, Theoretical study of aerosol particle electroscavenging by clouds, Journal of Aerosol Science 135 (2019) 1–20. doi:https://doi.org/10.1016/j.jaerosci.2019.04.001.
URL https://www.sciencedirect.com/science/article/pii/S0021850218304609

[23] J. Nuvoli, S. Bourrous, F.-X. Ouf, D. Thomas, Measurement of the porosity of a pseudo-spherical nanostructured particle deposit formed by filtration, Journal of Aerosol Science 151 (2021) 105681. doi:https://doi.org/10.1016/j.jaerosci.2020.105681.
URL https://www.sciencedirect.com/science/article/pii/S0021850220301671

[24] G. Van Rossum, F. L. Drake, Python 3 Reference Manual, CreateSpace, Scotts Valley, CA, 2009.

[25] C. R. Harris, K. J. Millman, S. J. van der Walt, R. Gommers, P. Virtanen, D. Cournapeau, E. Wieser, J. Taylor, S. Berg, N. J. Smith, R. Kern, M. Picus, S. Hoyer, M. H. van Kerkwijk, M. Brett, A. Haldane, J. F. del Río, M. Wiebe, P. Peterson, P. Gérard-Marchant, K. Sheppard, T. Reddy, W. Weckesser, H. Abbasi, C. Gohlke, T. E. Oliphant, Array programming with NumPy, Nature 585 (7825) (2020) 357–362. doi:10.1038/s41586-020-2649-2.
URL https://doi.org/10.1038/s41586-020-2649-2

[26] P. Virtanen, R. Gommers, T. E. Oliphant, M. Haberland, T. Reddy, D. Cournapeau, E. Burovski, P. Peterson, W. Weckesser, J. Bright, S. J.

van der Walt, M. Brett, J. Wilson, K. J. Millman, N. Mayorov, A. R. J. Nelson, E. Jones, R. Kern, E. Larson, C. J. Carey, İ. Polat, Y. Feng, E. W. Moore, J. VanderPlas, D. Laxalde, J. Perktold, R. Cimrman, I. Henriksen, E. A. Quintero, C. R. Harris, A. M. Archibald, A. H. Ribeiro, F. Pedregosa, P. van Mulbregt, SciPy 1.0 Contributors, SciPy 1.0: Fundamental Algorithms for Scientific Computing in Python, Nature Methods 17 (2020) 261–272. doi:10.1038/s41592-019-0686-2.

[27] U. Ayachit, The ParaView Guide: A Parallel Visualization Application, Kitware Inc., 2015.

Appendix A. Contact angle probability density function in diffusion regime

. A theoretical contact angle probability density function f_D was obtained in diffusion regime. The situation understudy is represented in figure A.14. To obtain f_D we assume that the moving particle moves in every directions with no preferred one and can collide with the deposited particle on all its outer surface. We then study the ratio of the number of positions corresponding to an contact angle interval to the total number of possible positions.

. For a deposited particle of radius R_D and a moving particle of radius R_M, all the possible positions of the center of the moving particle at collision lie on a sphere of radius $R = R_M + R_D$. Our post-processing way gives the absolute value of the contact angles. Therefore, here we only consider half of the sphere for which $\theta \geqslant 0$. The total surface containing the initial position just prior to capture area is:

$$S_T = 2\pi R^2; \qquad \text{with} \qquad R = R_M + R_D \tag{A.1}$$

The area of the differential surface $\mathrm{d}S$ containing the positions just prior to capture, which corresponds to contact angles between θ and $\theta + \mathrm{d}\theta$ follows from Pappus' centroid theorem in differential form:

$$\mathrm{d}S(\theta) = \int_{\phi=0}^{\phi=\frac{\pi}{2}} r\left(\theta\right) \sqrt{\left(\frac{\mathrm{d}r}{\mathrm{d}\theta}\right)^2 + \left(\frac{\mathrm{d}z}{\mathrm{d}\theta}\right)^2}\, \mathrm{d}\theta \tag{A.2}$$

$$r\left(\theta\right) = R\cos\left(\theta\right); \qquad \text{with} \qquad R = R_M + R_D \tag{A.3}$$

$$z\left(\theta\right) = R\sin\left(\theta\right); \qquad \text{with} \qquad R = R_M + R_D \tag{A.4}$$

$$\mathrm{d}S(\theta) = 2\pi R^2 \cos\left(\theta\right) \mathrm{d}\theta \tag{A.5}$$

The probability density is the variation of the probability p with θ.

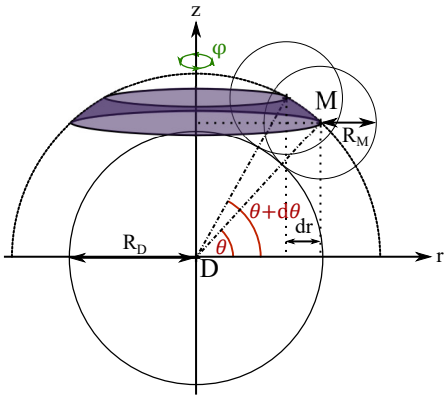

Figure A.14: Schematic of the system considered to obtain the probability density function of contact angles in diffusion regime.

$$\frac{\mathrm{d}p}{\mathrm{d}\theta} = \frac{1}{S_T}\frac{\mathrm{d}S(\theta)}{\mathrm{d}\theta} = \frac{2\pi R^2 \cos(\theta)}{2\pi R^2} = \cos(\theta) \tag{A.6}$$

The probability density function can thus be written:

$$\begin{array}{rccc} \mathrm{f_D} & : & \left[0, \frac{\pi}{2}\right] & \rightarrow & [0,1] \\ & & \theta & \mapsto & \cos(\theta) \end{array} \tag{A.7}$$

. From the probability density function the expected value, $E_D[\theta]$ of the contact angle in diffusion regime can be computed.

$$E_D[\theta] = \int_0^{\frac{\pi}{2}} \theta f_D(\theta)\,\mathrm{d}\theta = \int_0^{\frac{\pi}{2}} \theta \cos(\theta)\,\mathrm{d}\theta \tag{A.8}$$

Integration by parts then yields :

$$E_B[\theta] = \frac{\pi}{2} - 1\ rad = 32.7^{\,o} \tag{A.9}$$

Appendix B. Contact angle probability density function in ballistic regime

A theoretical contact angle probability density function f_B was obtained in ballistic regime. The situation understudy is represented in figure B.15. To obtain f_B the probability of capture of a spherical particle by a another one is studied. The following assumption were made :

- the traveling particle is dropped from a plane P_D;
- the traveling particle moves in straight line in the direction of the normal, $\boldsymbol{N}$, to the drop plane.

The set of initial positions of the moving particle leading to capture by the deposited particle is a disk, with an area of :

$$S_T = \pi \left(R_D + R_M\right)^2 \tag{B.1}$$

where R_D is the radius of the deposited particle and R_M the radius of the moving particle. The moving particle is initially placed at random on this disk. The probability that the moving particle collides with the deposited particle at a contact angle within $[\theta, \theta + \mathrm{d}\theta]$, is here noted $\mathrm{d}p$. $\mathrm{d}p$ is the ratio of the surface containing the initial positions of the moving particle leading to a capture within those limits, $\mathrm{d}S(\theta)$, to the surface of the entire disk, S_T :

$$\mathrm{d}p = \frac{\mathrm{d}S(\theta)}{S_T} = \frac{2\pi r \mathrm{d}r}{\pi \left(R_M + R_D\right)^2} \tag{B.2}$$

With:

$$r = \cos(\theta)\left(R_M + R_D\right) \tag{B.3}$$

$$\mathrm{d}r = -\sin(\theta)\left(R_M + R_D\right)\mathrm{d}\theta \tag{B.4}$$

As we are interested in the variation in area and not on whether it is a reduction or an increase, we take the absolute value:

$$\frac{\mathrm{d}p}{\mathrm{d}\theta} = 2\cos(\theta)\sin(\theta) = \sin(2\theta) \tag{B.5}$$

The probability density function is therefore given by equation (B.6).

$$\begin{array}{rcccc} \mathrm{f_B} & : & \left[0, \frac{\pi}{2}\right] & \rightarrow & [0,1] \\ & & \theta & \mapsto & \sin(2\theta) \end{array} \tag{B.6}$$

. From the probability density function the expected value, $E_B\left[\theta\right]$ of the contact angle in ballistic regime can be computed.

$$E_B\left[\theta\right] = \int_0^{\frac{\pi}{2}} \theta f_B\left(\theta\right) \mathrm{d}\theta \int_0^{\frac{\pi}{2}} \theta \sin\left(2\theta\right) \mathrm{d}\theta \tag{B.7}$$

Integration by parts then yields :

$$E_B\left[\theta\right] = \frac{\pi}{4}\ rad = 45\ ^o \tag{B.8}$$

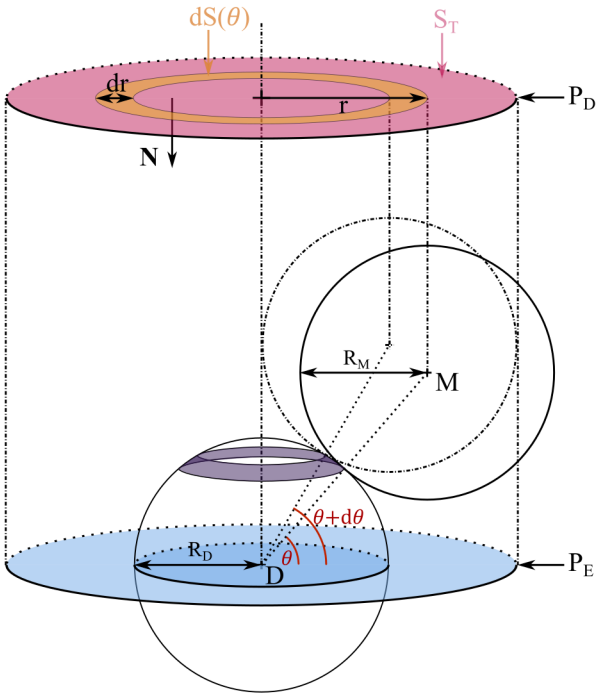

Figure B.15: Schematic of the system considered to obtain the probability density function of contact angles in ballistic regime.

Appendix C. Contact angles for tilted streamlines

. Here are gathered the contact angles obtained with the different α values.

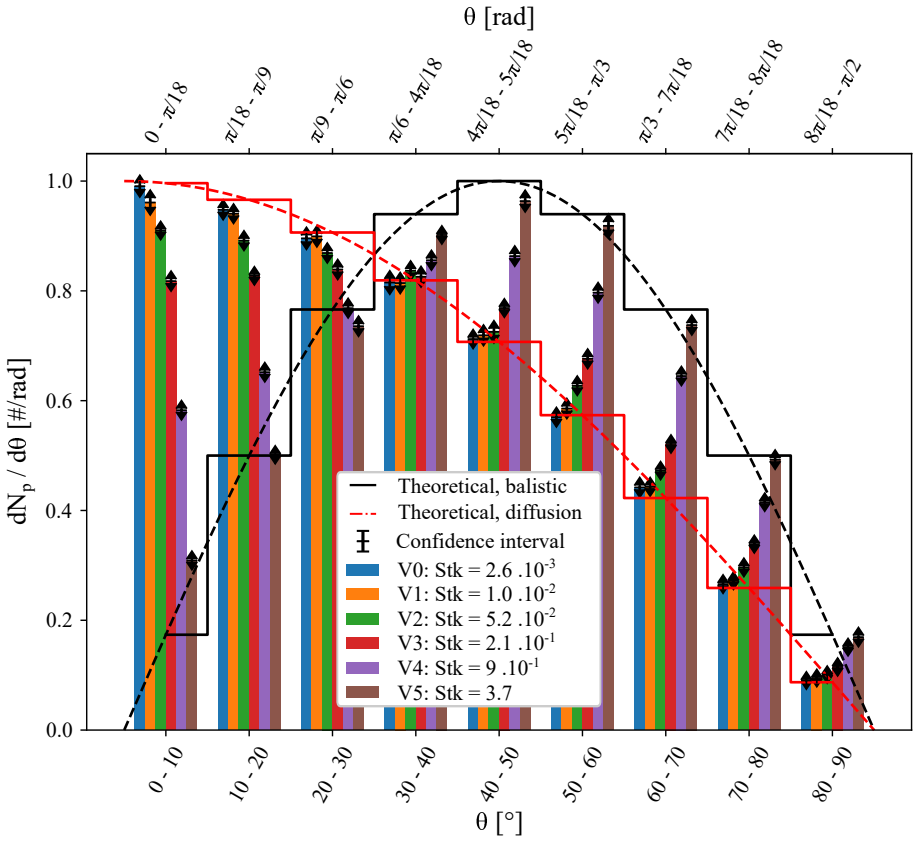

Figure C.16: Contact angles histogram for simulations conducted using CsCl particles with $\alpha = 5\ ^{o}$.

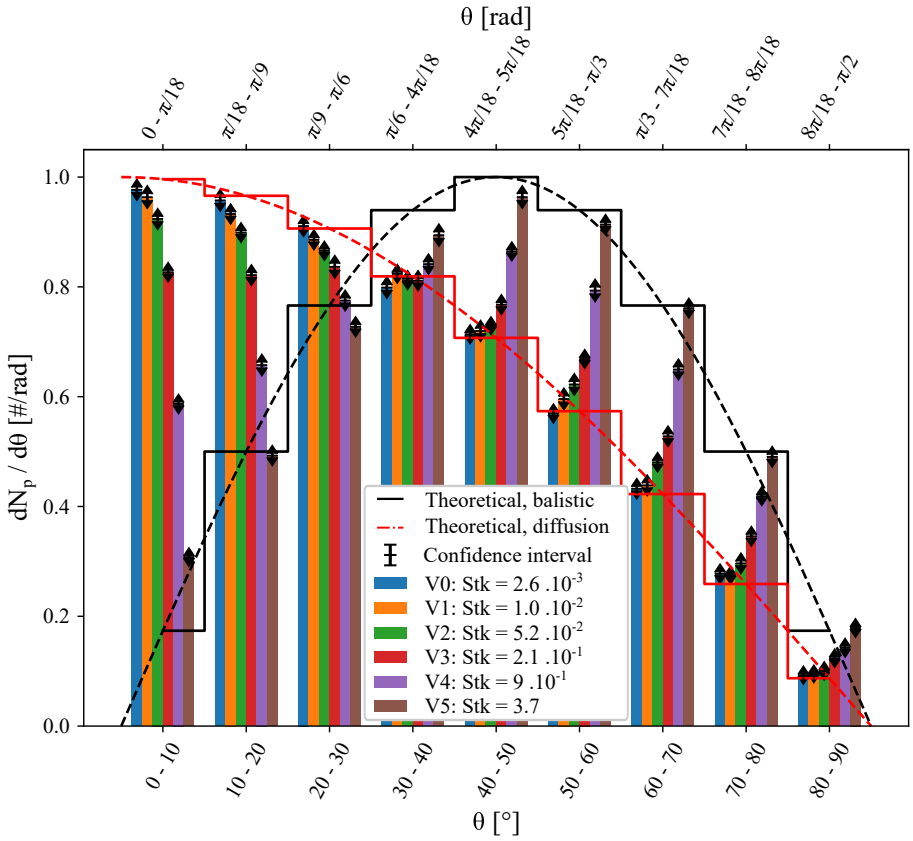

Figure C.17: Contact angles histogram for simulations conducted using CsCl particles with $\alpha = 15\ ^o$.

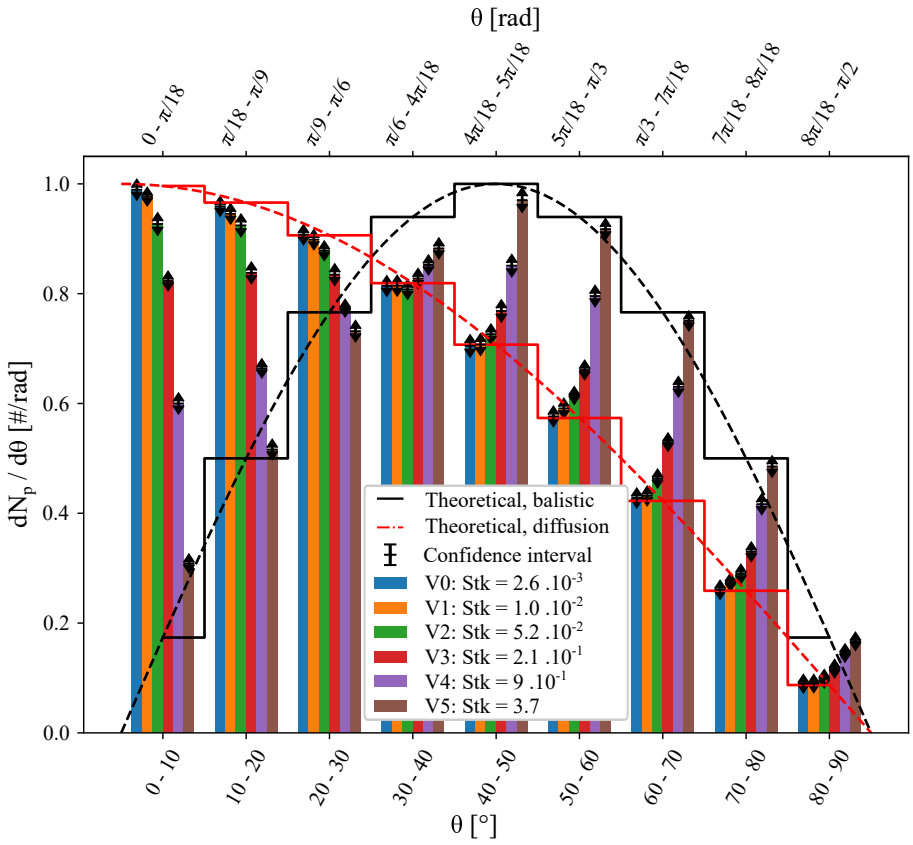

Figure C.18: Contact angles histogram for simulations conducted using CsCl particles with $\alpha = 30\ ^o$.

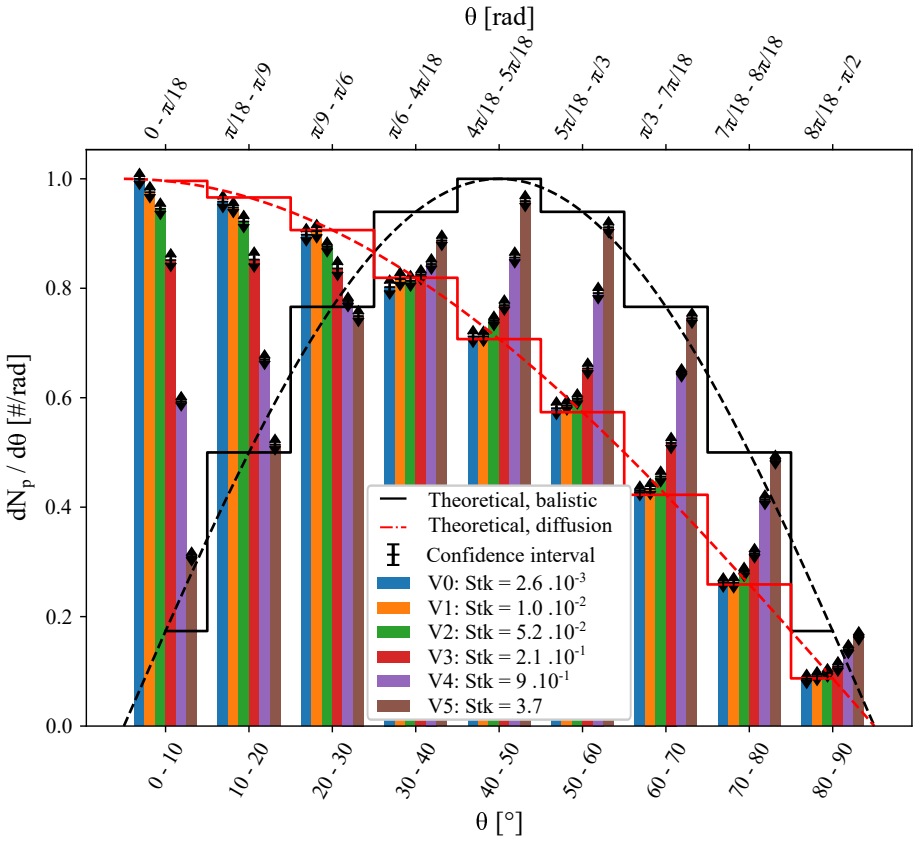

Figure C.19: Contact angles histogram for simulations conducted using CsCl particles with $\alpha = 45\ ^o$.

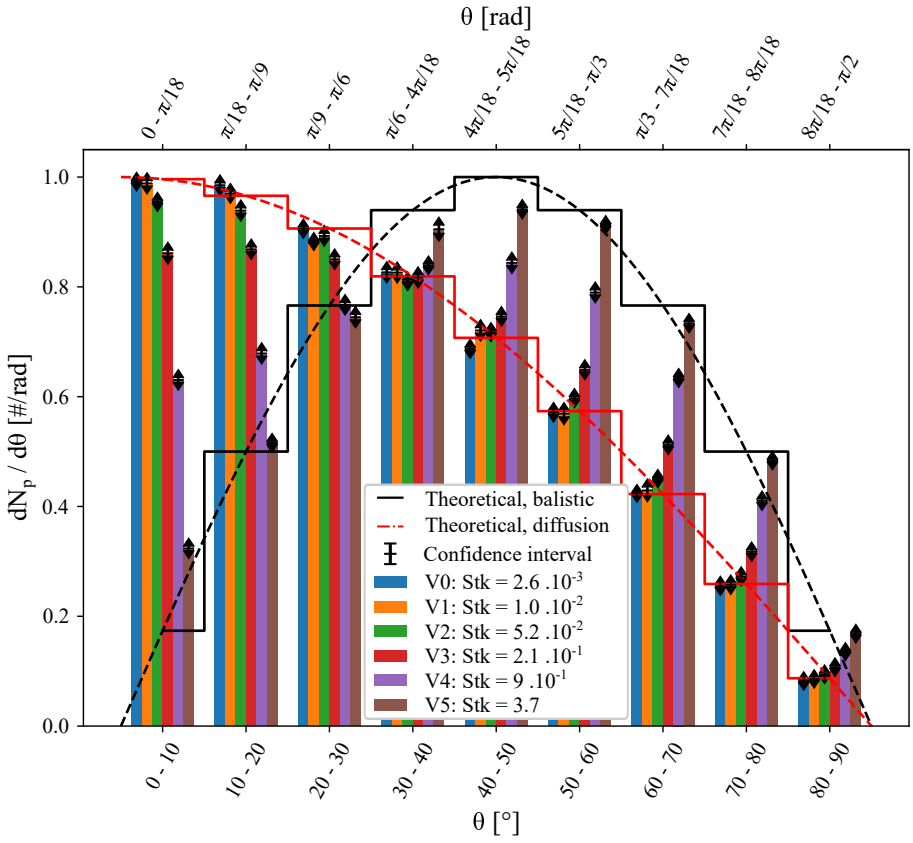

Figure C.20: Contact angles histogram for simulations conducted using CsCl particles with $\alpha = 60\ ^o$.

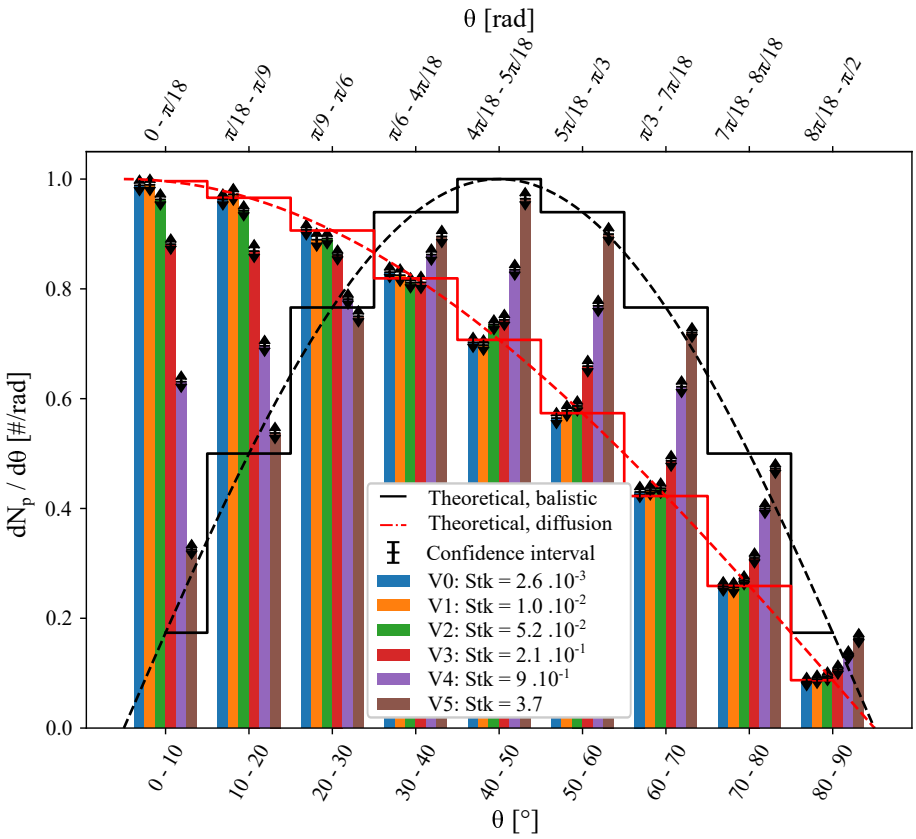

Figure C.21: Contact angles histogram for simulations conducted using CsCl particles with $\alpha = 75\ ^{o}$.

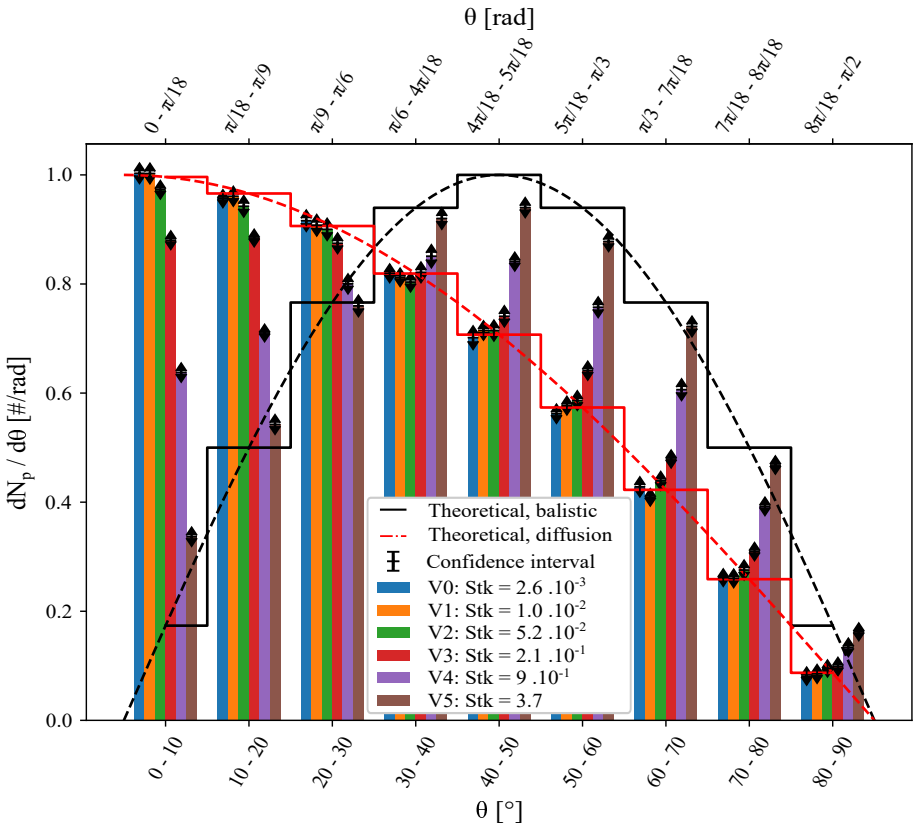

Figure C.22: Contact angles histogram for simulations conducted using CsCl particles with $\alpha = 85\ ^o$.

Appendix D. Coordination numbers for tilted streamlines

. Here are gathered the contact angles obtained with the different α values.

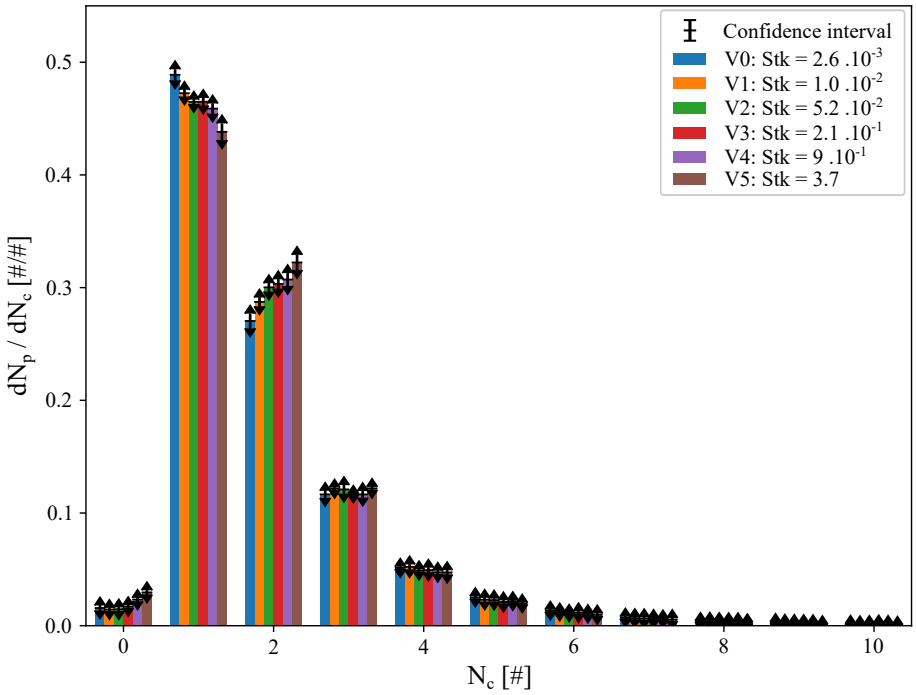

Figure D.23: Coordination numbers histogram for simulations conducted using CsCl with $\alpha = 5\ ^{o}$. Parts of the histograms with $N_c > 10$ were left out.

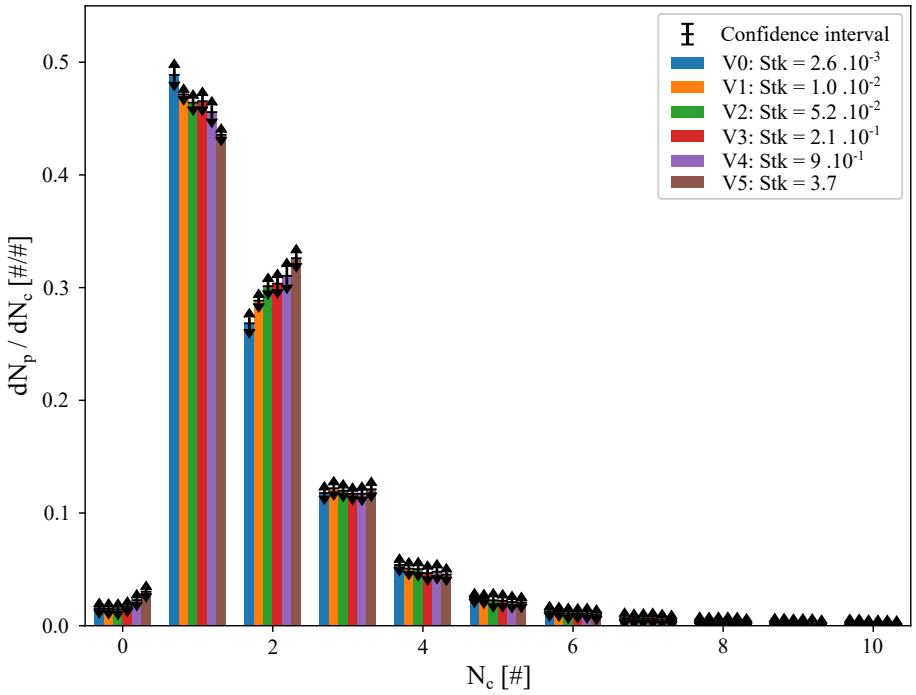

Figure D.24: Coordination numbers histogram for simulations conducted using CsCl with $\alpha = 15\ ^o$. Parts of the histograms with $N_c > 10$ were left out.

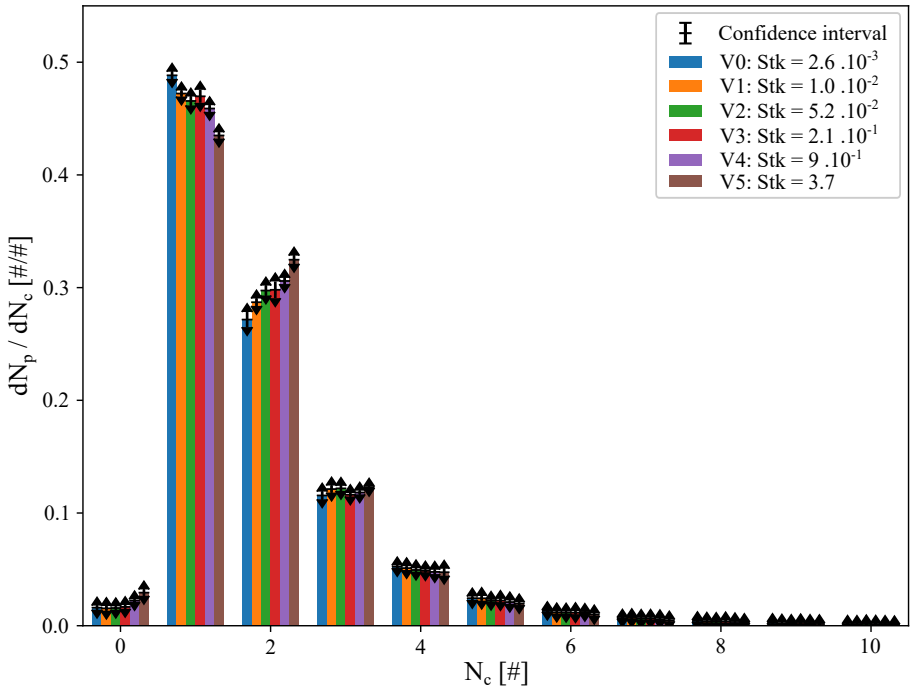

Figure D.25: Coordination numbers histogram for simulations conducted using CsCl with $\alpha = 30\ ^o$. Parts of the histograms with $N_c > 10$ were left out.

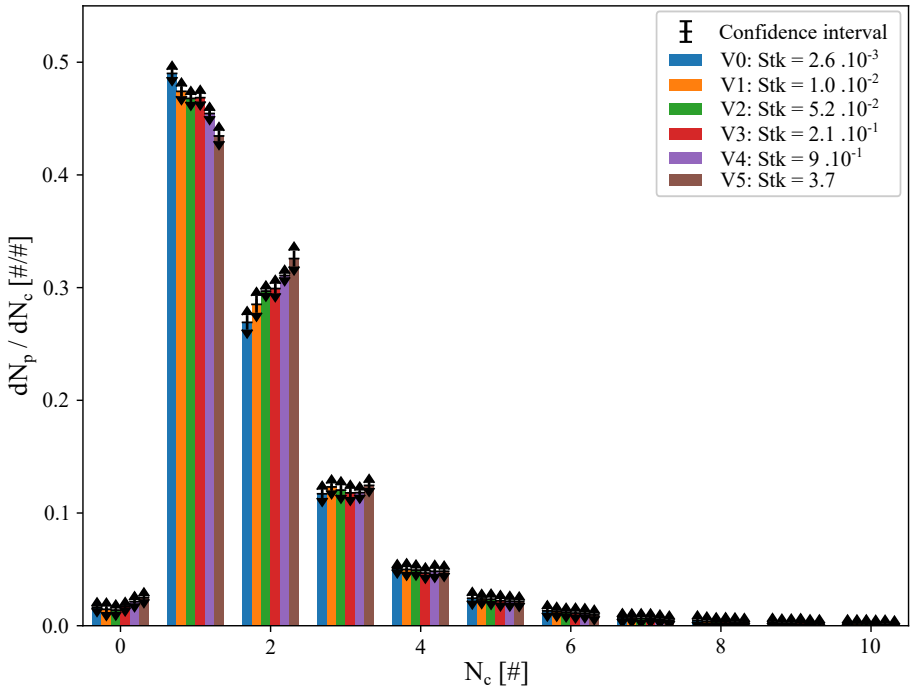

Figure D.26: Coordination numbers histogram for simulations conducted using CsCl with $\alpha = 45\ ^o$. Parts of the histograms with $N_c > 10$ were left out.

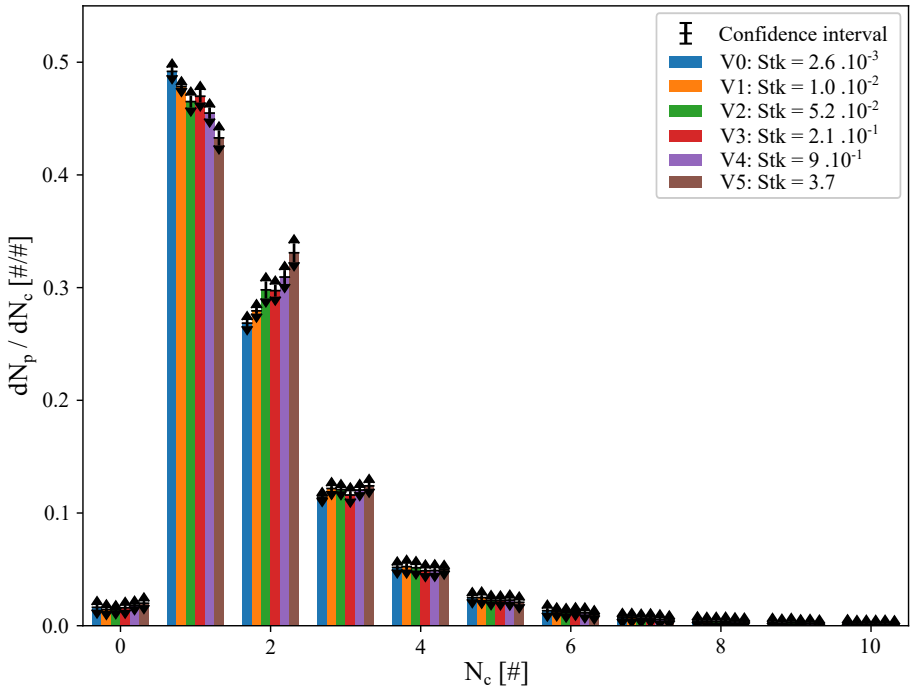

Figure D.27: Coordination numbers histogram for simulations conducted using CsCl with $\alpha = 60\ ^o$. Parts of the histograms with $N_c > 10$ were left out.

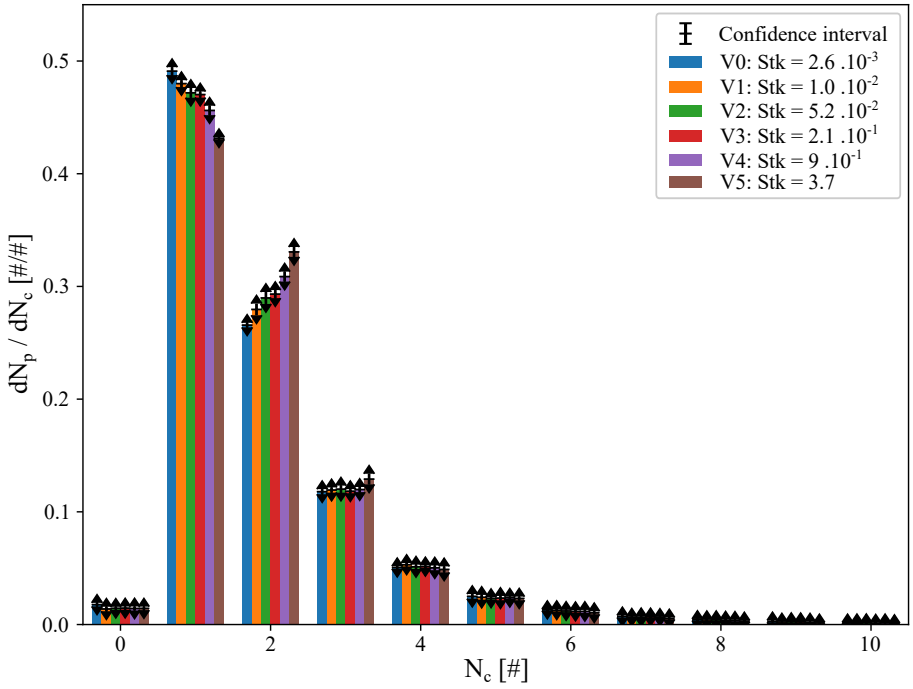

Figure D.28: Coordination numbers histogram for simulations conducted using CsCl with $\alpha = 75\ ^o$. Parts of the histograms with $N_c > 10$ were left out.

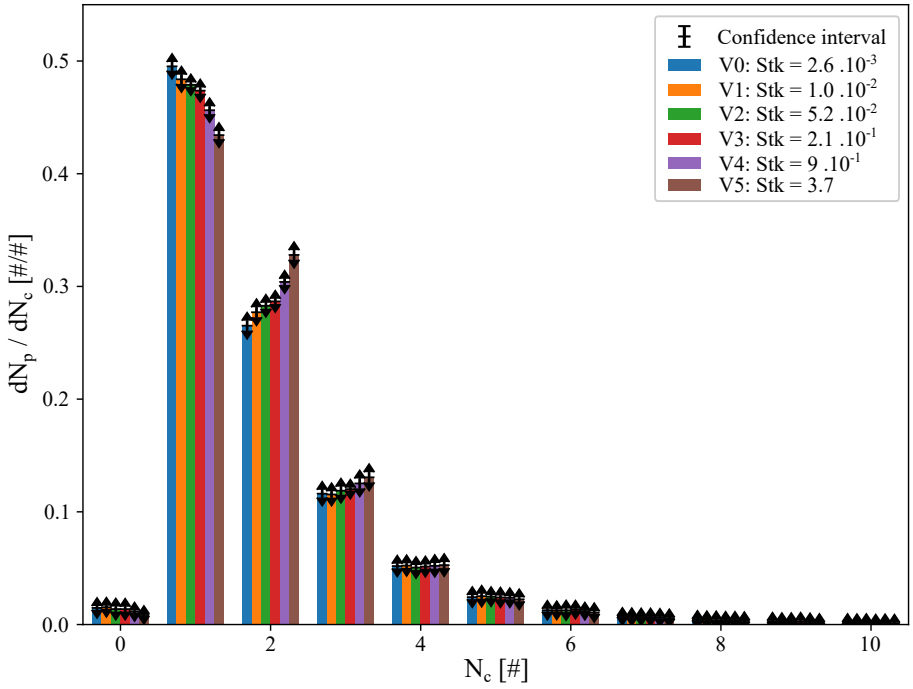

Figure D.29: Coordination numbers histogram for simulations conducted using CsCl with $\alpha = 85\ ^o$. Parts of the histograms with $N_c > 10$ were left out.